nature communications

Article

https://doi.org/10.1038/s41467-025-57497-z

Dynamic synthesis and transport of phenazine-1-carboxylic acid to boost extracellular electron transfer rate

Received: 26 April 2023

Accepted: 24 February 2025

Feng Li[1,6], Baocai Zhang[1,2,6], Xizi Long[3], Huan Yu[1,2], Sicheng Shi[1], Zixuan You[1], Qijing Liu[1], Chao Li[1], Rui Tang[1], Shengbo Wu[1], Xingjuan An[1], Yuanxiu Li[1], Liang Shi[4], Kenneth H. Nealson[5] & Hao Song[1,2] ✉

Electron shuttle plays a decisive role in extracellular electron transfer (EET) of exoelectrogens. However, neither identifying the most efficient electron shuttle molecule nor programming its optimal synthesis level that boosts EET has been established. Here, the phenazine-1-carboxylic acid (PCA) biosynthesis pathway is first constructed to synthesize PCA at an optimal level for EET in *Shewanella oneidensis* MR-1. To facilitate PCA transport, the porin OprF is expressed to improve cell membrane permeability, the cytotoxicity of which, however, impaired cell growth. To mitigate cytotoxicity, PCA biosensor is designed to dynamically decouple PCA biosynthesis and transport, resulting in the maximum output power density reaching 2.85 ± 0.10 W m^{-2}, 33.75-fold higher than wild-type strain. Moreover, extensive analyses of cellular electrophysiology, metabolism, and behaviors reveal PCA shuttles electrons from cell to electrode, which is the dominant mechanism underlying PCA-boosted EET. We conclude dynamic synthesis and transport of PCA is an efficient strategy for enhancing EET.

Electroactive microorganisms (EAMs) have extracellular electron transfer (EET) capabilities that underlie a diverse array of bio-electrochemical systems (BESs)[1–3], including microbial fuel cells for simultaneous environmental treatment (wastewater treatment[4,5] and bioremediation[6,7]) and power generation (bioelectricity[5,8,9] and biohydrogen[10,11]), microbial electrosynthesis for the production of value-added chemicals[12,13], biofuels[14,15], inorganic nanomaterials[16,17] and polymers[18–20]. In addition, EAMs were used as key components of next-generation bio-electronics to power wearable/implantable devices and contrive microscale biosensing for real-time environmental and health monitoring[21–23]. However, the low EET rate with limited current and power production remains a crucial bottleneck that restricts BESs from adoption in practical applications.

EAMs employ membrane-associated *c*-type cytochromes (*c*-Cyts)[24], conductive nanowires[25,26] as electron conduits for direct EET pathway, and/or redox-active small molecules[27–30] as electron shuttles for indirect EET pathway. The EET pathways mediate electron flow from metabolically produced intracellular electrons to extracellular electron acceptors. To enhance the EET rate, a number of approaches have been developed to engineer the molecular components involved in EET, including *c*-type cytochromes, conductive nanowires, and electron shuttles[31]. In particular, many EAMs employed electron shuttles to capture electrons from redox-active proteins on cell membrane or intracellular oxidoreductase to facilitate EET via redox cycles[32–34], which was thus feasible to be an efficient engineering target for promoting EET.

---

[1]State Key Laboratory of Synthetic Biology, and School of Chemical Engineering and Technology, Tianjin University, Tianjin 300072, China. [2]College of Life and Health Sciences, Northeastern University, Shenyang 110169, China. [3]Hunan Province Key Laboratory of Typical Environmental Pollution and Health Hazards, School of Public Health, Hengyang Medical School, University of South China, Hengyang, Hunan 421001, China. [4]Department of Biological Sciences and Technology, School of Environmental Studies, China University of Geoscience in Wuhan, Wuhan, Hubei 430074, China. [5]Departments of Earth Science & Biological Sciences, University of Southern California, 4953 Harriman Ave., South Pasadena, CA 91030, USA. [6]These authors contributed equally: Feng Li, Baocai Zhang. ✉e-mail: songhao@mail.neu.edu.cn

The performances of both naturally occurred and artificially synthesized redox-active compounds in BESs were studied via exogenous addition or enhanced endogenous biosynthesis[35,36]. While many of these electron shuttles can be used by EAMs to facilitate EET, such as flavins for *Shewanella*[29,37], *Geobacter*[38], and *Listeria*[39], phenazines for *Pseudomonas*[27,40,41], and quinones for *Aeromonas*[42] and *Shewanella*[43], their efficacies in enhancing EET were dependent upon structure and concentration. For example, Simoska et al. studied the EET of *Escherichia coli* mediated by phenazine derivatives (including neutral red, pyocyanin, and phenazine-1-carboxamide, etc.) at various concentrations, suggesting that their efficacies in promoting EET exhibited marked distinctions[36]. In combination with experimental data, they conducted mathematical modeling to elucidate the structure-function relationship in phenazine-mediated EET[44], revealing the effective molecular structure of phenazine in EET of *E. coli*. However, it remained elusive the optimal redox-active shuttle molecule (such as phenazines, flavins, or quinones) and its concentration that conferred efficient EET to the model exoelectrogen, *Shewanella oneidensis*.

In this work, the efficient electron shuttle phenazine-1-carboxylic acid (PCA) underlying EET of *Shewanella oneidensis* MR-1, a well-studied model exoelectrogen, is screened from electron shuttles including phenazines, flavins, and quinones. This inspires us to investigate whether programming the PCA-mediated EET pathway in *S. oneidensis* could enhance current generation, the synthetic biology engineering strategy of which is detailed in Supplementary Fig. 1 and Supplementary Note 1. Firstly, to synthesize PCA at the optimal concentration, PCA de novo biosynthesis pathways are constructed in *S. oneidensis* MR-1 via mining the PCA biosynthetic operons and using genetic regulation tools to optimize gene expression. Secondly, to facilitate PCA transport, a PCA biosensor P_{soxR}-*soxR*-P_{soxS} with appropriate sensitivity and response strength is developed to dynamically initiate the expression of the porin OprF based on sensing the intracellular PCA concentration, which relieves cytotoxicity caused by the premature expression of OprF and improves cell permeability. The dynamic synthesis and transport of PCA promotes the EET rate of the engineered *S. oneidensis* with a maximum output power density of 2.85 ± 0.10 W m^{-2}, 33.75-fold higher than that of the wild-type (WT) *S. oneidensis* MR-1. Finally, analyses of cellular electrophysiology, metabolism (electron donor catabolism and *c*-Cyts biosynthesis), and behavior (biofilm formation) reveal the dominant mechanism underlying the PCA-boosted EET. The intracellularly biosynthesized PCA is transported out of cell by OprF, subsequently undergoing reduction by the outer membrane *c*-Cyts MtrC and OmcA and shuttling electrons to electrode, thus accelerating EET. This study demonstrates that dynamic synthesis and transport of PCA is an efficient strategy to promote EET of *S. oneidensis*.

Results

Construction and optimization of the PCA biosynthesis pathway in *S. oneidensis*

Using *S. oneidensis* MR-1, we found that the addition of PCA at ~80 μM resulted in the highest power generation, which was significantly higher than that of either flavins or quinones when added at their optimal levels, respectively (Fig. 1a and Supplementary Figs. 2–5). Meanwhile, PCA exhibited an optimal level in mediating EET of *S. oneidensis* MR-1. As shown in Fig. 1b, the EET rate increased as the amount of added PCA increased in the beginning, while the EET rate peaked at the PCA concentration of ~80 μM and a further increase in PCA concentration resulted in suboptimal EET. This result suggested that the PCA level needed to be maintained at ~80 μM (an optimal level as an electron shuttle) to promote EET.

To establish a PCA biosynthesis pathway (Supplementary Fig. 6) and maintain the PCA level at ~80 μM in *S. oneidensis* MR-1, the native PCA biosynthesis operons *phzABCDEFG* from nine phenazine-producing species of four different genera[45] (*Streptomyces. cinnamonensis* DSM1042 in *Streptomyces* (I), *Burkholderia lata* 383 in *Burkholderia* (II), *Erwinia. carotovora* ssp. *Atroseptica* SCRI1043 in *Pectobacterium* (III), and *Pseudomonas. aeruginosa* PA14, *P. aeruginosa* PAO1, *P. fluorescens* 2-79, *P. aureofaciens* 30-84, *P. chlororaphis* GP72, *P. chlororaphis* PCL1391 in *Pseudomonas* (IV)), were individually cloned into *S. oneidensis* MR-1 driven by the promoter P_{lacUV5}, resulting in eleven recombinant strains SC1-SC11 (Fig. 1c, Supplementary Fig. 1, Supplementary Note 1, and Supplementary Data 1). Three strains (SC1, SC3, and SC11) that harbored the three PCA synthesis operons from *S. cinnamonensis* DSM1042, *E. carotovora* ssp. *Atroseptica* SCRI1043, and *P. chlororaphis* PCL1391 were unable to elicit PCA synthesis, while the other eight recombinant strains were capable of synthesizing detectable levels of PCA. Notably, the operons from *Pseudomonas* genera (*P. aeruginosa* PA14, *P. aeruginosa* PAO1, *P. fluorescens* 2-79, and *P. aureofaciens* 30-84) showed relatively high activity for synthesizing PCA. Strain SC7 bearing the operon *phzABCDEFG* from the PCA biosynthesis gene cluster in *P. aeruginosa* PAO1 produced the highest PCA level of 8.72 ± 0.76 μM (Fig. 1c). The EET rates of these strains were positively correlated with the synthesized PCA level, and strain SC7 (P_{lacUV5}-*phzABCDEFG*) enabled the highest EET rate with the maximum power density of 1185.93 ± 63.46 mW m^{-2}, 14.07-fold increase over WT (84.30 ± 2.53 mW m^{-2}) (Fig. 1d and Supplementary Fig. 7). Strain SC7 was thus chosen for further analysis (Supplementary Fig. 1, Supplementary Note 1, and Supplementary Data 1).

To improve PCA synthesis, the promoter that drives the operon *phzABCDEFG* was optimized to upregulate the operon expression level in strain SC7. Six promoters (P_{arcA}, P_{ae}, P_{laps}, P_{tac}, P_{T7}, and P_{xyl}) with *gfp* as a reporter gene were tested in *S. oneidensis* MR-1, revealing that P_{ae}, P_{xyl}, and P_{tac} were stronger than P_{lacUV5} (Supplementary Fig. 8), and these three promoters were then individually assembled into strain SC7 to replace the promoter P_{lacUV5}, resulting in three recombinant strains SO1-SO3 (Fig. 1e, Supplementary Fig. 1, Supplementary Note 1, and Supplementary Data 1). Strains SO2 and SO3 exhibited higher PCA levels than that of strain SC7 (Fig. 1e). Notably, strain SO3 (P_{tac}-*phzABCDEFG*) containing the P_{tac}-driven *phzABCDEFG* operon from *P. aeruginosa* PAO1 produced PCA at a level of 72.74 ± 4.30 μM (Fig. 1e), close to the optimal PCA level (~80 μM), which resulted in a maximum output power density of 1757.87 ± 28.91 mW m^{-2}, 1.48-fold increase than that of strain SC7 (1185.93 ± 63.46 mW m^{-2}) (Fig. 1f and Supplementary Fig. 7). Thus, strain SO3 was selected for further study (Supplementary Fig. 1, Supplementary Note 1, and Supplementary Data 1).

Engineering cell membrane permeability to facilitate PCA transport

To enhance EET rate, the intracellular PCA has to be transported out of cells in time, and it has been known that cellular permeability plays an important role in transmembrane transport of electron shuttles[46]. Thus, aiming to increase the cell membrane permeability of strain SO3 to facilitate PCA transport, the genes of outer membrane (OM) porin and inner membrane (IM) efflux pump were individually incorporated in *S. oneidensis* to regulate the porin-mediated passive diffusion and the efflux pump-mediated active transport of PCA, respectively (Fig. 2a).

Six OM porins were individually expressed in strain SO3: OprF from *P. aeruginosa* PAO1, OmpPst1 from *Providencia stuartii*, OmpF from *E. coli* K12, OmpC from *E. coli* K12, Omp35 from *Klebsiella. pneumoniae*, and Omp36 from *K. pneumoniae*. A dual-plasmid system was used, in which the PCA biosynthesis operon *phzABCDEFG* driven by the promoter P_{tac} was expressed in the plasmid pYYD, and the porin gene driven by the promoter P_{lacUV5} was expressed in the other plasmid pHG13, eventually resulting in six strains SP1-SP6 (Fig. 2b, Supplementary Fig. 1, Supplementary Note 1, and Supplementary Data 1). In these six strains, strain SP1 (P_{tac}-*phzABCDEFG* and P_{lacUV5}-*oprF*) exhibited the highest power density (2262.45 ± 10.92 mW m^{-2}), 1.29-fold higher than that of SO3 (Fig. 2b and Supplementary Fig. 9).

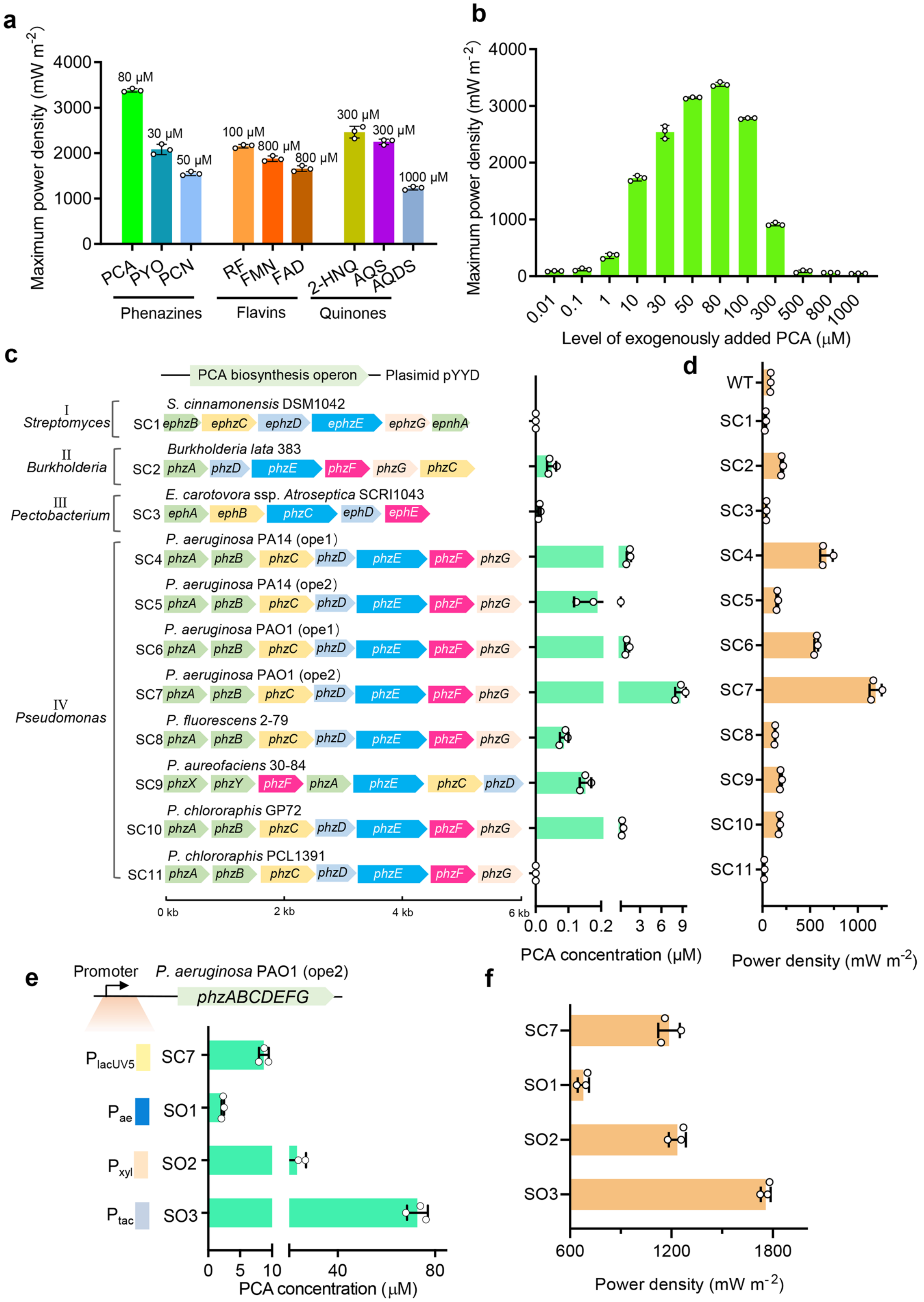

In addition, we individually expressed four IM efflux pumps (PA3718 from *P. aeruginosa* PA14, MexG from *P. aeruginosa* PAO1, PA3523 from *P. aeruginosa* PAO1, and Bfe from *S. oneidensis* MR-1), resulting in four strains SP7-SP10 (Fig. 2b, Supplementary Fig. 1, Supplementary Note 1, and Supplementary Data 1). However, these strains with the IM efflux pumps exhibited lower EET than that of strain SO3. Strain SP1 was thus used for further study (Supplementary Fig. 1, Supplementary Note 1, and Supplementary Data 1).

To verify whether OprF enhanced cell envelope permeability to facilitate PCA transport and consequently increased the EET rate, we conducted an N-phenyl-1-naphthylamine (NPN) uptake assay to evaluate the cell membrane permeability. The non-polar NPN molecule

Fig. 1 | Construction and optimization of PCA biosynthesis pathway in *S. oneidensis* for synthesizing PCA at the optimal concentration. a Maximum output power density of *S. oneidensis* MR-1 by exogenously adding 80 μM PCA, 30 μM PYO (Pyocyanin), 50 μM PCN (Phenazine-1-carboxamide), 100 μM RF (Riboflavin), 800 μM FMN (Flavin mononucleotide), 800 μM FAD (Riboflavin adenine dinucleotide), 300 μM 2-HNQ (2-hydroxy-1,4-naphoquinone), 300 μM AQS (Sodium anthraquinone-2-sulfonate), and 1000 μM AQDS (Anthraquinone-2,6-disulfonate), respectively. **b** Maximum output power density of *S. oneidensis* MR-1 with exogenously added PCA at various concentrations. **c** PCA biosynthesis operons originated from the primary phenazine producers in members of four genera: *Streptomyces* (I), *Burkholderia* (II), *Pectobacterium* (III), and *Pseudomonas* (IV) driven by the promoter P_{lacUV5} (Left panel), and the synthesized PCA level by strains SC1-SC11 (Right panel). **d** Maximum output power density of the strains SC1-SC11. **e** PCA synthesis enhancement via promoter engineering. The left panel displayed the promoters (P_{lacUV5}, P_{ae}, P_{xyl}, and P_{tac}). The right panel showed the synthesized PCA level driven by the corresponding promoter. **f** Maximum power density of the strains SO1-SO3. Maximum power densities were taken from power density profiles in Supplementary Figs. 3–5 and 7. Results from three independent experiments ($n = 3$) were expressed as means and standard errors. Data in (**a**–**f**) are shown as the mean ± SD. Source data are provided as a Source Data file.

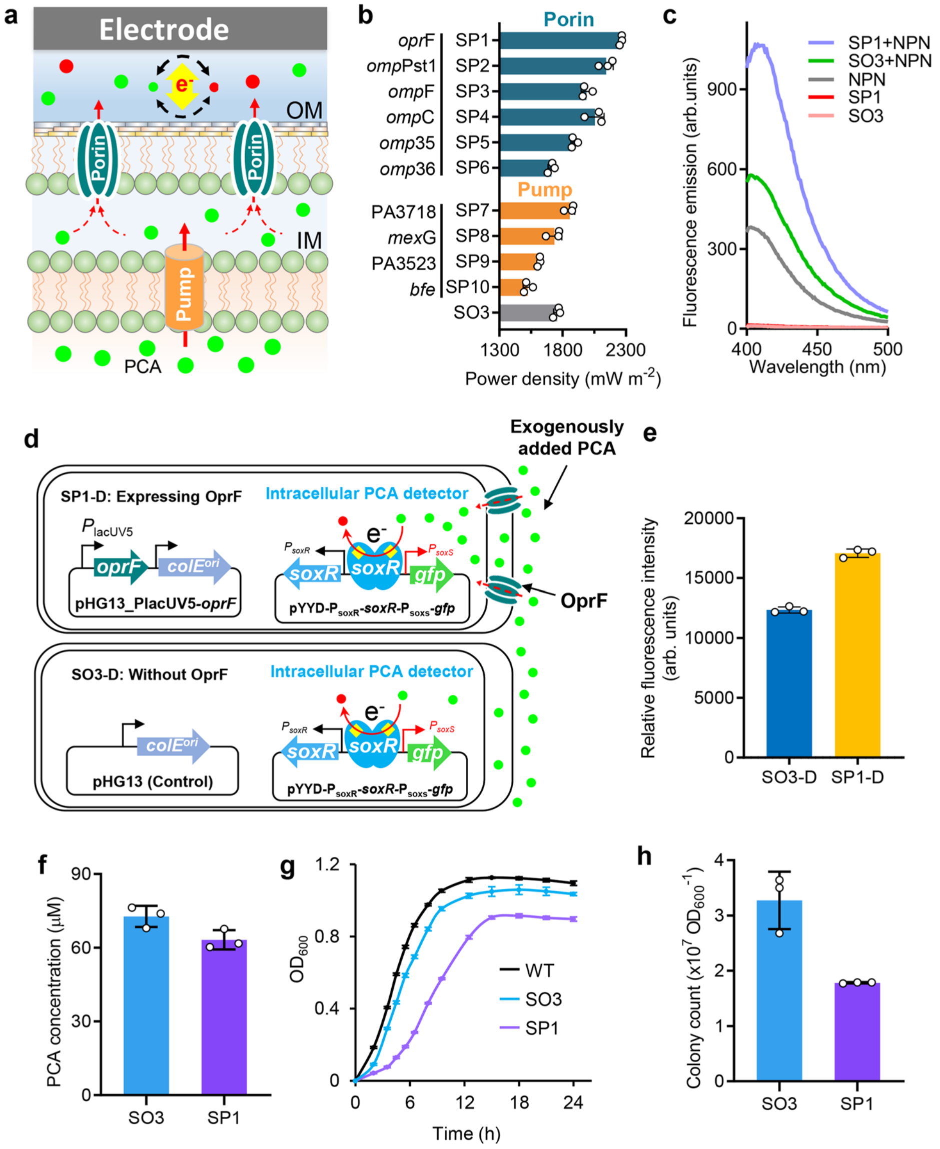

Fig. 2 | Engineering cell membrane permeability to facilitate PCA transport in *S. oneidensis*. a Schematic of cell membrane permeability consisting of porin-mediated passive diffusion in the outer membrane (OM) and efflux pump-mediated active transport in the inner membrane (IM). **b** Maximum power density (taken from Supplementary Fig. 9) of strains SP1-SP6 and SP7-SP10. **c** NPN uptake assay to measure cell permeability (arb. units: arbitrary units). **d** Schematic of the intracellular PCA detector (pYYD-P_{soxR}-*soxR*-P_{soxS}-*gfp*) for evaluating cellular membrane permeability to PCA. The redox stress-responsive sensor P_{soxR}-*soxR*-P_{soxS} was employed to develop an intracellular PCA detector, comprising the effector protein SoxR and the SoxR-regulated promoter P_{soxS}. In P_{soxR}-*soxR*-P_{soxS}, the [2Fe-2S] cluster within SoxR dimer could be oxidized by PCA to activate the transcription of P_{soxS}. Upon exogenous introduction of PCA to a strain containing the PCA detector but lacking the PCA biosynthesis operon, the externally supplied PCA is transported into the cell, thereby activating GFP expression. This transport process is positively correlated with cellular membrane permeability. Consequently, cellular membrane permeability to PCA can be assessed by measuring the relative fluorescence intensity of GFP. **e** The relative fluorescence intensity of GFP. **f** The synthesized PCA level. **g** Cell growth profiles. **h** The viable cell number assessed from the dilution plate method. Results in (**b**–**h**) from three independent experiments ($n = 3$) were expressed as means and standard errors, and data in (**b**–**h**) are shown as the mean ± SD. The result (**c**) has been checked for consistency with 3 individual experiments. Source data are provided as a Source Data file.

would emit strong fluorescence when diffusing from the aqueous solution into non-polar cellular phospholipids. When the above strains were mixed with NPN, the SP1 + NPN mixture showed a stronger fluorescence intensity than that of SO3 + NPN (Fig. 2c), suggesting NPN in strain SP1 was higher than in strain SO3, an indication that strain SP1 possessed higher cell membrane permeability than that of strain SO3.

Given the difference in the molecular structure of PCA and NPN, to evaluate cellular membrane permeability to PCA molecule, we developed an intracellular PCA detector (pYYD-P_{soxR}-*soxR*-P_{soxS}-*gfp*) based on the redox stress-responsive biosensor P_{soxR}-*soxR*-P_{soxS}, which consists of the effector protein SoxR driven by the constitutive promoter P_{soxR} and the promoter P_{soxS} regulated by SoxR (Fig. 2d). In P_{soxR}-*soxR*-P_{soxS}, the SoxR dimer binds to the promoter P_{soxS}, in which the [2Fe-2S] cluster of SoxR can be oxidized by PCA, leading to change in SoxR conformation, thus activating the transcription of P_{soxS}[47,48]. Upon exogenously supplying PCA to the strain harboring the PCA detector (pYYD-P_{soxR}-*soxR*-P_{soxS}-*gfp*) but lacking the PCA biosynthesis operon, the externally supplied PCA is transported into the cell to activate the GFP expression, and the PCA transport is positively correlated with the cellular membrane permeability, which thus enables evaluation of cellular membrane permeability to PCA by measuring the relative fluorescence intensity of GFP. As shown in Fig. 2e, exogenous addition of PCA (80 μM) to the culture medium resulted in the relative fluorescence intensity of 17076.10 ± 356.18 arbitrary units (arb. units) for strain SP1-D (pYYD-P_{soxR}-*soxR*-P_{soxS}-*gfp* & pHG13-PlacUV5-*oprF*), which was 1.38-fold higher than that of strain SO3-D (pYYD-P_{soxR}-*soxR*-P_{soxS}-*gfp* & pHG13) (12353.93 ± 259.50 arb. units). This result suggests that more PCA molecules could be transported into the cell with OprF expression, thus demonstrating increased cellular membrane permeability to PCA in strain SP1 compared to strain SO3.

However, in comparison with strain SO3, the level of PCA in strain SP1 was slightly decreased from 72.74 ± 4.30 μM (SO3) to 63.23 ± 3.91 μM (SP1) (Fig. 2f), and strain SP1 exhibited a significant decrease in growth rate compared to strain SO3 and WT (Fig. 2g). We further assessed the viable cell number via colony-forming units (CFU). As shown in Fig. 2h, the number of viable cells was $3.27 \pm 0.52 \times 10^7$ for strain SO3, 1.84-fold higher than that of strain SP1 ($1.78 \pm 0.01 \times 10^7$), indicating the lower cell viability of strain SP1 than that of strain SO3. These results suggested that overexpression of OprF inhibited cell growth and impaired cell viability.

Upon transcription and translation in cytoplasm, the porin OprF (a membrane protein) is transported and inserted into the cell membrane via the signal recognition particle pathway[49] and the Sec-translocon[50,51]. A previous study showed that overexpression of exogenous membrane protein would overload the Sec-translocon system due to its limited capacity, thus inducing cytotoxicity[52]. Specifically, when the expression level of an exogenous membrane protein (e.g., OprF in *S. oneidensis* MR-1) exceeds the transport capacity of the Sec-translocon system, it creates bottlenecks in protein sorting and translocation, leading to intracellular misfolding and aggregation of both OprF precursors and other membrane protein precursors in cytoplasm. The misfolding and aggregation of protein precursors would disrupt cellular homeostasis and trigger stress response of the cells. In addition, the accumulation of OprF at high levels would inhibit the proper insertion and folding of other essential endogenous membrane proteins, thus inhibiting cell growth. Consequently, OprF expression facilitates PCA transmembrane transport to accelerate EET, while its cytotoxicity would impair cell growth and viability.

Dynamic decoupling PCA biosynthesis and transport relieved OprF-induced cytotoxicity

To relieve OprF cytotoxicity, we designed a dynamic regulatory approach to decouple PCA transport and biosynthesis. In the initial phase (low PCA level), the cell synthesized PCA without expressing the porin OprF; when PCA accumulated to a certain threshold level, as sensed by the PCA biosensor, OprF expression was then initiated to facilitate PCA transport. In this way, the cellular metabolic processes were not inhibited in the early phase of cell growth due to silencing of the *oprF* gene. This allowed effective cell growth and PCA synthesis. By the time OprF overexpression commenced, the cell growth had reached the exponential growth phase, and the cellular machineries responsible for endogenous membrane protein synthesis, translocation, insertion, and folding were already established, thereby mitigating the cytotoxicity caused by the excessive OprF expression.

To this end, the redox stress responding sensor P_{soxR}-*soxR*-P_{soxS} was further used to regulate the expression of the *oprF* gene. It was found that the GFP expression level was correlated with the added PCA level (Supplementary Fig. 10), suggesting that P_{soxR}-*soxR*-P_{soxS} could act as the PCA biosensor for sensing the PCA level. The gene circuit P_{soxR}-*soxR*-P_{soxS}-*oprF* was constructed in the plasmid pHG13 and transferred into strain SO3, resulting in the recombinant strain SD1 (P_{tac}-*phzABCDEFG* and P_{soxR}-*soxR*-P_{soxS}-*oprF*) that harbored the PCA synthesis operon P_{tac}-*phzABCDEFG* in the plasmid pYYD (pYYD-PCA), and the PCA biosensor-regulated transport circuit P_{soxR}-*soxR*-P_{soxS}-*oprF* in the plasmid pHG13 (pHG13-*soxR*-P_{soxS}-*oprF*) (Fig. 3a, top row; Supplementary Fig. 1, Supplementary Note 1, and Supplementary Data 1). In this way, strain SD1 possessed the capacity of dynamic regulation of PCA transport based upon sensing the intracellular PCA level, of which the EET rate was further assessed.

However, strain SD1 exhibited an unexpectedly lower output power density of 1797.64 ± 53.40 mW m^{-2} than its parental strain SP1 (2262.45 ± 10.92 mW m^{-2}) (Fig. 3b and Supplementary Fig. 11), suggesting that the OprF expression under the control of the wild-type PCA biosensor impeded EET. To reveal the differential expression of OprF in strains SP1 and SD1, the corresponding expression levels were quantified by fusing green fluorescent protein (GFP) to OprF, resulting in P_{lacUV5}-*oprF-gfp* in strain SP1 and P_{soxR}-*soxR*-P_{soxS}-*oprF-gfp* in strain SD1. We found that the time and intensity of the GFP expression under the control of P_{soxR}-*soxR*-P_{soxS} in strain SD1 were much delayed and lower than in strain SP1 under the control of the promoter P_{lacUV5} (Fig. 3c), explaining the tardiness and weakness of OprF expression in SD1, which incapacitated PCA transport, thus inhibiting the EET rate of strain SD1.

To address this issue, we developed a site-specific mutagenesis approach to optimize the PCA biosensor to achieve appropriate response strength and sensitivity. In the PCA-biosensor P_{soxR}-*soxR*-P_{soxS}, the SoxR dimer binds to the 19 bp binding sites located between the -35 and -10 elements of the promoter P_{soxS}. When SoxR is oxidized by PCA, its redox-dependent conformation is then altered, which results in DNA twist of the promoter P_{soxS} and allows RNA polymerase to bind to P_{soxS} to initiate the transcription of the downstream genes[48]. Therefore, the DNA sequence of the promoter P_{soxS}, acting as the SoxR binding site, plays a decisive role in the sensitivity of the PCA biosensor. We conducted single-, two-, and multi-base mutations in the SoxR DNA binding site in the promoter P_{soxS}, resulting in nine PCA biosensor variants P_{soxR}-*soxR*-P_{soxS} V1 - P_{soxR}-*soxR*-P_{soxS} V9, respectively (as shown in Fig. 3a, bottom row). By replacing the wild-type PCA biosensor P_{soxR}-*soxR*-P_{soxS} with the nine PCA biosensor variants in strain SD1, respectively, nine recombinant strains SDV1-SDV9 were obtained (Supplementary Fig. 1, Supplementary Note 1, and Supplementary Data 1). Bio-electrochemical characterizations of these strains showed that strain SDV3 (P_{tac}-*phzABCDEFG* and P_{soxR}-*soxR*-P_{soxS} V3-*oprF*) exhibited the highest EET rate with the maximum power density of 2845.26 ± 100.19 mW m^{-2}, 1.26-fold higher than that of strain SP1 (2262.45 ± 10.92 mW m^{-2}) (Fig. 3b and Supplementary Fig. 11), which, to the best of our knowledge, is one of the highest recorded power outputs by a recombinant exoelectrogen[3,9,53,54]. Strain SDV3 was thus chosen for further study (Supplementary Fig. 1, Supplementary Note 1, and Supplementary Data 1).

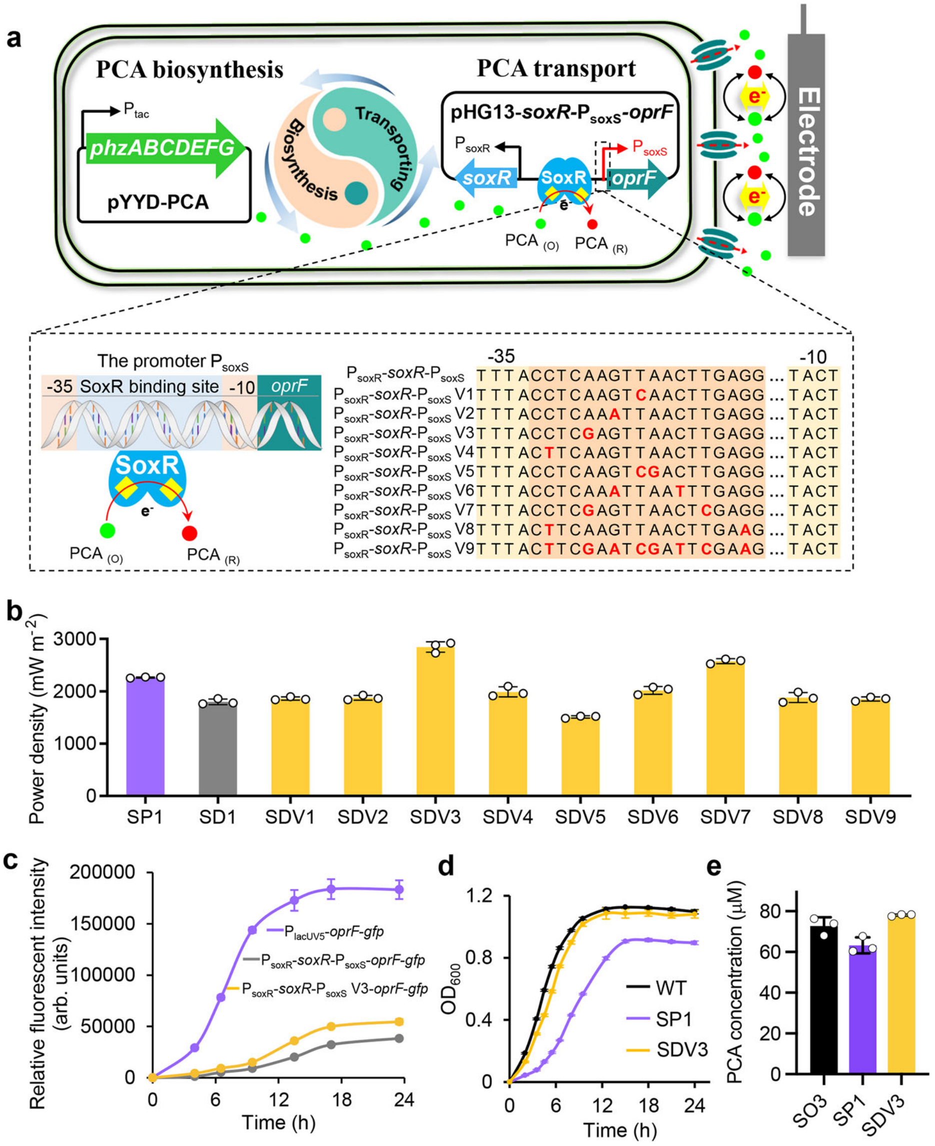

Fig. 3 | Dynamic decoupling of PCA biosynthesis and transport to relieve OprF cytotoxicity and resolve OprF-impaired cell growth of *S. oneidensis*. **a** Schematic of dynamic decoupling of PCA biosynthesis with transport (top row) and optimization of PCA biosensor (bottom row). The PCA biosensor P_{soxR}-*soxR*-P_{soxS} consisted of effector protein SoxR driven by constitutive promoter P_{soxR}, and promoter P_{soxS} regulated by SoxR, in which SoxR dimer bound with promoter P_{soxS} and its [2Fe-2S] cluster could be oxidized by PCA, leading to the change of SoxR conformation, thus activating transcription of P_{soxS}. In strain SD1 harboring the PCA synthesis operon P_{tac}-*phz*ABCDEFG in pYYD (pYYD-PCA) and the PCA biosensor-regulated transport circuit P_{soxR}-*soxR*-P_{soxS}-*oprF* in pHG13 (pHG13-*soxR*-P_{soxS}-*oprF*) (top row), cell first synthesized PCA driven by operon P_{tac}-*phzABCDEFG*, then initiated OprF porin expression under the control of gene circuit P_{soxR}-*soxR*-P_{soxS}-*oprF* to achieve programmed PCA biosynthesis and transport. In the optimization of PCA biosensor (bottom row), site-specific mutagenesis was conducted in the SoxR DNA binding site, locating between the -35 and -10 elements in the promoter P_{soxS} of wild-type PCA biosensor (P_{soxR}-*soxR*-P_{soxS}), resulting in nine PCA biosensor variants P_{soxR}-*soxR*-P_{soxS} V1-V9, respectively. **b** Maximum power density (taken from Supplementary Fig. 11) of the strains SD1 and SDV1-SDV9. **c** The *oprF* gene expression profiles regulated by the promoters P_{lacUV5} in SP1, P_{soxR}-*soxR*-P_{soxS} in strain SD1, and P_{soxR}-*soxR*-P_{soxS} V3 in strain SDV3, respectively. **d** Cell growth curves of strains WT, SP1, and SDV3. **e** The synthesized PCA level. Results in (**b**–**e**) from three independent experiments ($n = 3$) were expressed as means and standard errors, and data in (**b**–**e**) are shown as the mean ± SD. Source data are provided as a Source Data file.

In addition, the gene expression profile under the control of the PCA biosensor variant P_{soxR}-*soxR*-P_{soxS} V3 (P_{soxR}-*soxR*-P_{soxS} V3-*oprF-gfp* in SDV3, Fig. 3c) showed that the *oprF* expression time and intensity in strain SDV3 were earlier and higher than those in strain SD1 (P_{soxR}-*soxR*-P_{soxS}-*oprF-gfp* in SD1), but still slower and significantly lower than those in SP1 (P_{lacUV5}-*oprF-gfp* in SP1). This observation suggested that the response strength and sensitivity of the PCA biosensor variant P_{soxR}-*soxR*-P_{soxS} V3 was optimized in regulating the OprF expression. As shown in Fig. 3d, the growth rate and the final OD_{600} of strain SDV3 were similar to WT and higher than strain SP1, which showed the OprF cytotoxicity in strain SP1 was resolved in strain SDV3. Also, the biosynthesized PCA level in strain SDV3 was recovered from 63.23 ± 3.91 μM (SP1) to 78.08 ± 0.50 μM (SDV3) (Fig. 3e). Thus, the PCA biosensor-based approach to dynamically decouple PCA synthesis and transport relieved cytotoxicity caused by the OprF overexpression, enabling the synthesis of PCA at a level to achieve high output power density.

Elucidating molecular mechanisms of PCA-boosted EET

PCA shuttled electrons from OM c-Cyts MtrC and OmcA to electrode. A previous study showed that the electron shuttle as redox mediator could receive electrons from outer membrane *c*-type cytochromes (OM

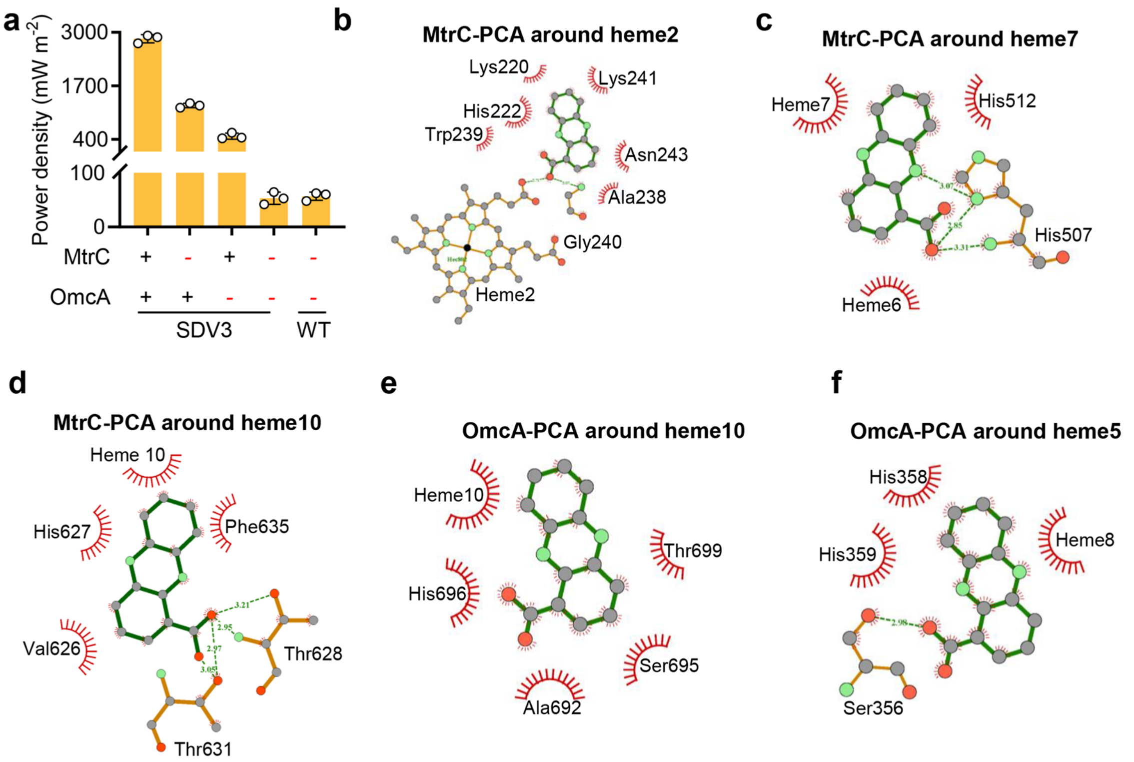

Fig. 4 | Electrophysiological analyses of PCA-boosted EET in *S. oneidensis*. **a** Maximum output power density (taken from Supplementary Fig. 12) of the *c*-Cyts deletion mutants, including SDV3 (MtrC^{+}OmcA^{+}), SDV3Δ*mtrC* (MtrC^{-}OmcA^{+}), SDV3Δ*omcA* (MtrC^{+}OmcA^{-}), SDV3Δ*mtrC*Δ*omcA* (MtrC^{-}OmcA^{-}), and WTΔ*mtrC*Δ*omcA* (MtrC^{-}OmcA^{-}). **b**–**f** Interactions in the complexes of PCA-MtrC (**b**–**d**) and PCA-OmcA (**e**, **f**) were analyzed, in which hydrogen bonds were shown as green dotted lines and non-bond interactions (e.g. hydrophobic interactions) were shown as red radial lines. The gray, green, red, and black balls represented carbon, nitrogen, oxygen, and iron atoms, respectively. Results in (**a**) from three independent experiments ($n = 3$) were expressed as means and standard errors, and data in (**a**) are shown as the mean ± SD. The results in (**b**–**f**) have been checked for consistency with 3 individual experiments. Source data are provided as a Source Data file.

c-Cyts), which subsequently shuttled these electrons to electrode[34]. To elucidate how electrons were transferred from strain SDV3 to PCA molecules, the genes *mtrC* and *omcA* encoding the OM *c*-Cyts MtrC and OmcA were thus individually or simultaneously deleted in SDV3 and WT, respectively. As shown in Fig. 4a and Supplementary Fig. 12, strains SDV3Δ*mtrC* (1221.94 ± 53.25 mW m^{-2}) and SDV3Δ*omcA* (474.52 ± 75.22 mW m^{-2}) showed 2.33- and 6.00-fold decrease in power density compared to strain SDV3 (2845.26 ± 100.19 mW m^{-2}), respectively. Moreover, SDV3Δ*mtrC*Δ*omcA* (53.15 ± 11.41 mW m^{-2}) displayed minimal power generation, similar to the strain WTΔ*mtrC*Δ*omcA* (56.87 ± 7.73 mW m^{-2}). These findings suggested the OM *c*-Cyts MtrC and OmcA were essential for PCA-mediated EET. Similarly to another phenazine derivative, phenazine methosulfate[55,56], PCA could almost completely oxidize both MtrC and OmcA in vitro (Supplementary Fig. 13 and Supplementary Note 2). These results revealed that electrons were transferred from the SDV3 cell to PCA through OM *c*-Cyts MtrC and OmcA.

The electron shuttles (flavins) in *Shewanella* were observed to either bind with OM *c*-Cyts as a cofactor or diffuse freely along the redox gradient potential[57–60]. To explore the interaction mechanism between OM *c*-Cyts (MtrC and OmcA) and PCA, differential pulse voltammetry (DPV) analysis was performed. The shifts in PCA peak potential (Supplementary Figs. 14–15 and Supplementary Note 3–4) and the variations in the PCA half-width potential (Supplementary Fig. 16 and Supplementary Note 5) suggested that PCA could function as a cofactor, binding with MtrC and OmcA to form complexes to facilitate EET at low concentrations. As the PCA concentration increased, the PCA binding sites within MtrC and OmcA became saturated, thus the excess PCA adopted the diffusion-based shuttling mechanism for EET.

To further investigate the specific binding sites involved in the interaction between PCA and MtrC/OmcA, we conducted computational molecular docking simulation. The hemes 2, 7, and 10 of MtrC and the hemes 5 and 10 of OmcA, located at the termini of multiheme wires[61–63], were thus selected as the box centers for docking simulation, respectively. The simulation results showed that PCA could form hydrogen bonds with residues Gly240, heme 2, His507, Thr628, and Thr631 in MtrC (Fig. 4b–d), and Ser356 in OmcA (Fig. 4f). In addition, PCA also formed non-bond interactions (e.g., hydrophobic interactions) with various residues in both MtrC (e.g., Lys220, His222, Trp239, Lys241, Asn243, His512, Val626, His627, Phe635, and hemes 6, 7, 10, etc. Fig. 4b–d) and OmcA (e.g., His358, His359, Ser695, His696, Thr699, and hemes 8, 10 etc. Fig. 4e, f). The shortest distances between the N5 atom of PCA and the iron atoms of heme 2, heme 7, and heme 10 in MtrC, as well as heme 5 and heme 10 in OmcA were measured to be 5.8, 6.2, 7.3, 5.8, and 6.8 Å, respectively (Supplementary Fig. 17 and Supplementary Table 1), which were all shorter than the maximum distance (11 Å) allowing for electron hopping to occur, indicating both MtrC and OmcA could transfer electrons to PCA via electron hopping from heme 2, heme 7 and/or heme 10 of MtrC, as well as heme 5 and/or heme 10 of OmcA.

To validate these simulation results, the dissociation constant (K_d) in the interactions between PCA and *c*-Cyts was calculated according to the protein-ligand binding model developed by Okamoto et al.[64] (Eqs. 1–4). Accordingly, the amino acids that interact with PCA in MtrC and OmcA were firstly individually mutated to alanine (Ala), thus constructing 19 *c*-Cyts Ala mutants (Supplementary Data 1). According to Eqs. 3 and 4, the estimated K_d value for PCA was 0.36 μM when interacting with the wild-type (WT) *S. oneidensis* MR-1 (Table 1 and Supplementary Fig. 18). In comparison, by interacting with *c*-Cyts mutants, the estimated K_d value for

Table 1 | The dissociation constant (K_d) in the interactions between PCA and cell strains

Strain	K_d (μM)	Fold (vs. WT)
Wild-type *S. oneidensis* MR-1(WT)	0.36	1.00
WT-MtrCLys220Ala	8.20	22.78
WT-MtrCHis222Ala	6.47	17.97
WT-MtrCTrp239Ala	1.35	3.75
WT-MtrCGly240Ala	0.80	2.22
WT-MtrCLys241Ala	2.50	6.94
WT-MtrCAsn243Ala	0.60	1.67
WT-MtrCHis507Ala	5.94	16.50
WT-MtrCHis512Ala	1.49	4.14
WT-MtrCVal626Ala	1.72	4.78
WT-MtrCHis627Ala	3.32	9.22
WT-MtrCThr628Ala	1.97	5.47
WT-MtrCThr631Ala	2.59	7.19
WT-MtrCPhe635Ala	8.00	22.22
WT-OmcASer356Ala	1.56	4.33
WT-OmcAHis358Ala	0.39	1.08
WT-OmcAHis359Ala	12.94	35.94
WT-OmcASer695Ala	6.00	16.67
WT-OmcAHis696Ala	1.31	3.64
WT-OmcAThr699Ala	4.31	11.97

Source data are provided as a Source Data file.

PCA was significantly increased. Especially for strains WT-MtrCLys220Ala (8.20 μM), WT-MtrCHis222Ala (6.47 μM), WT-MtrCLys241Ala (2.50 μM), WT-MtrCHis507Ala (5.94 μM), WT-MtrCHis627Ala (3.32 μM), WT-MtrCThr631Ala (2.59 μM), WT-MtrCPhe635Ala (8.00 μM), WT-OmcAHis359Ala (12.94 μM), WT-OmcASer695Ala (6.00 μM), and WT-OmcAThr699Ala (4.31 μM), the estimated K_d value was 22.78-, 17.97-, 6.94-, 16.50-, 9.22-, 7.19-, 22.22-, 35.94-, 16.67-, and 11.97-fold higher than that of the WT, respectively, indicating the disruption of these amino acid would hinder the binding of PCA with *c*-Cyts (MtrC and OmcA). Besides, the *c*-Cyts Ala mutants all showed decreased maximum power density (Supplementary Fig. 19 and Supplementary Note 6). These results thus collectively confirmed the molecular docking simulations.

PCA enhanced carbon source catabolism, *c*-Cyts biosynthesis, and biofilm formation. Transcriptomic analysis (Supplementary Figs. 20-21 and Supplementary Table 2) showed significant alteration in the expression of genes related to carbon catabolism (e.g., *gltA*, *SO_1053*), cytochromes biosynthesis (e.g., *mtrC*, *dmsAB*[65], *yceJ*[66], etc.), iron uptake/transport (e.g., *fbpA*[67]), c-di-GMP synthesis and degradation (e.g., *dgcS*[68]), cellular motility (e.g., *flgT*[69] and *pilV*[70]), cell energy and chemotaxis (e.g., *SO_1434*[71]), as well as prophages (e.g., *gpF* and *gp46*[72]) in strain SDV3 with synthesized PCA in comparison to the WT strain (Supplementary Fig. 22, Supplementary Note 7, and Supplementary Data 2). These processes were tightly associated with the lactate catabolism, *c*-Cyts biosynthesis, and biofilm formation, suggesting PCA could modulate *Shewanella* cellular metabolism and behavior.

As shown in Fig. 5a, strain SDV3 exhibited a higher lactate consumption rate than that of WT, indicating PCA accelerated carbon source metabolism to enhance intracellular electron generation. Additionally, with heme staining, the sodium dodecyl sulfate-polyacrylamide gel electrophoresis (SDS-PAGE) showed the bands corresponding to MtrC and OmcA in strain SDV3 were significantly broader than those in WT (Fig. 5b), indicating a significantly higher abundance of MtrC and OmcA in strain SDV3 than that in WT. Consistent with this observation, the results of Raman spectrum (Supplementary Fig. 23a and Supplementary Note 8) and UV-visible spectroscopy (Supplementary Fig. 23b and Supplementary Note 8) suggested that PCA facilitated the biosynthesis of MtrC and OmcA, thereby accelerating electron transmembrane transfer. Furthermore, the scanning electron microscopy (SEM) and confocal laser scanning microscope (CLSM) observations revealed that strain SDV3 exhibited a thicker biofilm with a higher cell density on electrode surface compared to those of WT (Fig. 5c). Quantitative assessment of biofilm biomass revealed the strain SDV3 biofilm reached 285.30 ± 4.12 μg cm^{-2}, 4.24-fold higher than that of the WT biofilm (67.28 ± 4.64 μg cm^{-2}) (Fig. 5d). And the viable cell number in the strain SDV3 biofilm was $8.47 \pm 0.95 \times 10^7$ cm^{-2}, 5.39-fold higher than that of the WT biofilm ($1.57 \pm 0.21 \times 10^7$ cm^{-2}) (Fig. 5d). Moreover, the electrochemical impedance spectroscopy (EIS) analyses revealed the charge-transfer resistance of the strain SDV3 biofilm was 2113.74 Ω, 9.35-fold lower than that of WT (19756.41 Ω, Fig. 5e), indicating PCA significantly improved the biofilm conductivity, leading to reduction in electron transfer resistance.

The aforementioned biochemical characterizations demonstrated that PCA enhanced lactate consumption, *c*-Cyts biosynthesis, and biofilm formation. However, the mechanism through which PCA modulated metabolism and behavior of *Shewanella* remained unclear. According to a previous study[73], the cyclic adenosine 3′, 5′-monophosphate (cAMP)-cyclic adenosine 3′, 5′-monophosphate receptor protein (CRP) complex could bind with the promoter regions of *mtrCAB* (encoding the outer membrane *c*-Cyts complex MtrCAB), *omcA*, *dld* (encoding D-lactate dehydrogenase), and *lldP* (encoding lactate transport protein) to stimulate their transcription, thus strengthening the *c*-Cyts biosynthesis and lactate catabolism. Meanwhile, the class III adenylate cyclase CyaC, which catalyzes cAMP synthesis from ATP, could regulate its catalytic activity in response to the changes in redox state[74]. We thus speculated that PCA could potentially enhance the synthesis of cAMP in strain SDV3, thus promoting lactate catabolism and *c*-Cyts biosynthesis. Subsequent analysis of intracellular cAMP levels in strains SDV3 and WT revealed a significantly higher concentration in strain SDV3 (3.65 ± 0.23 pmol mg^{-1} protein), representing a 2.74-fold increase compared to WT (1.33 ± 0.23 pmol mg^{-1} protein) (Fig. 5f). Through RT-qPCR analysis (Supplementary Fig. 24), the transcription levels of the genes *dld*, *lldP*, *mtrCAB*, and *omcA* were up-regulated in strain SDV3 compared to those of WT, further accounting for the enhanced lactate consumption and *c*-Cyts biosynthesis. Additionally, in the course of biofilm formation, a recent study reported that cAMP-CRP could directly interact with a putative c-di-GMP effector of BpfD in *Shewanella*[75]. This interaction between cAMP-CRP and BpfD could strengthen the existing interaction between BpfD and protease BpfG, ultimately inhibiting the proteolytic activity and releasing a cell surface-associated adhesin of BpfA, thereby promoting biofilm formation[75]. In summary, a model of PCA-enhanced cellular metabolism and biofilm formation in *S. oneidensis* was refined (Fig. 5g). In strain SDV3, the synthesized PCA facilitated synthesis of cAMP, which bound with its receptor protein (CRP) to form a complex. The cAMP-CRP complex activated the transcription of the genes encoding *c*-Cyts (*mtrCAB*, and *omcA*) and enzymes (*dld* and *lldP*) involved in lactate catabolism. The elevated level of cAMP also promoted the release of the cell surface-associated adhesin BpfA, thereby facilitating biofilm formation.

The dominant mechanism underlying PCA-boosted EET was elucidated. It was shown PCA not only mediated electron transfer acting as an electron shuttle, but also improved cellular metabolism and biofilm formation, both of which could contribute to the increased EET rate. To further identify the dominant mechanism of the PCA-boosted EET, we inoculated strain SDV3 with its synthesized PCA in the three-electrode BES system poised at 0.24 V (*vs.* standard hydrogen electrode). A stable oxidation current density of 443.53 μA cm^{-2} was observed after 32 h′ incubation (stage I, Fig. 5h). Upon transfer of the SDV3 cells into a new medium in the absence of the inducer IPTG, PCA

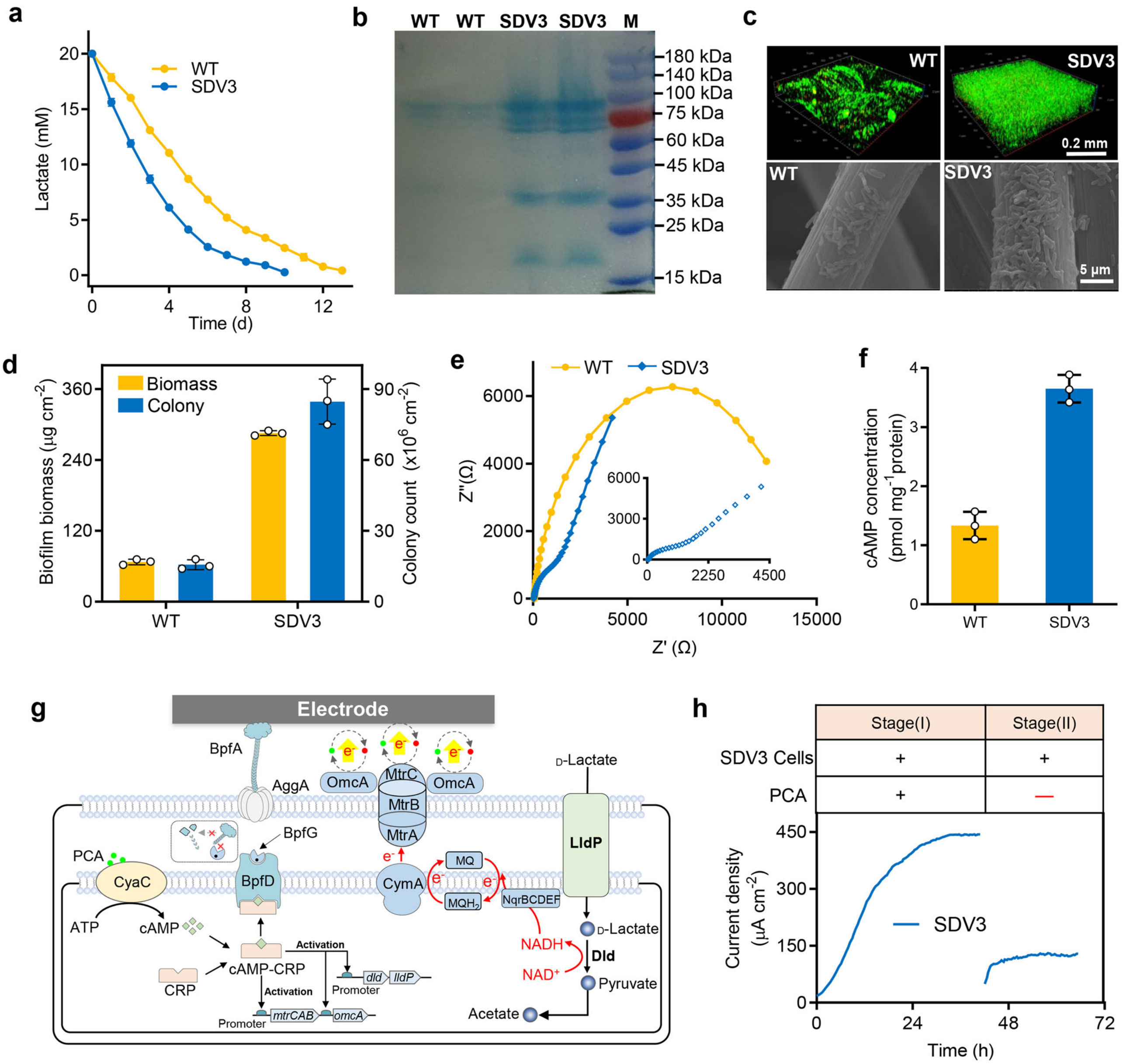

Fig. 5 | Analyses of PCA-modulated metabolism and biofilm formation of *S. oneidensis*. **a** Lactate consumption. **b** Sodium dodecyl sulfate polyacrylamide gel electrophoresis (SDS-PAGE) with heme staining. **c** CLSM (upper row) and SEM (bottom row) images of anodic biofilms. Scale bars of SEM and CLSM images were 5 μm and 0.2 mm, respectively. For gel and micrographs, the reported results have been checked for consistency with 3 individual experiments. **d** Assay of biomass and colony-forming units (CFU) of viable cells attached on anode surfaces. **e** Nyquist plot of electrochemical impedance spectroscopy. **f** The cyclic adenosine 3′, 5′-monophosphate (cAMP) levels in strains SDV3 and WT. **g** Mechanisms on PCA-enhanced cellular metabolism and biofilm formation of *S. oneidensis*. In strain SDV3, the synthesized PCA enhances cAMP synthesis and improves the level of intracellular cAMP. The increased cAMP binds with CRP forming a complex, which activates the transcription of *dld*, *lldP*, *mtrCAB*, and *omcA*, thereby regulating the lactate catabolism and *c*-Cyts biosynthesis. In addition, cAMP-CRP complex binds with BpfD, thus facilitating the interaction of BpfD with protease BpfG, which reduced proteolytic processing of adhesin, BpfA, thus enhancing release of BpfA and biofilm formation. Abbreviations: cAMP cyclic adenosine 3′, 5′-monophosphate, CRP cyclic adenosine 3′, 5′-monophosphate receptor protein, MQ methyl naphthoquinone, ATP adenosine triphosphate, CyaC class III adenylate cyclase, MtrC and OmcA decaheme *c*-Cyts, MtrB β-barrel trans-OM protein, MtrA periplasmic decaheme *c*-Cyts, CymA inner membrane tetraheme *c*-Cyts, Dld D-lactate dehydrogenase, LldP lactate transport protein, NqrBCDEF Na^+-translocating NADH-quinone reductase, BpfA cell surface-associated adhesin, AggA type I protein secretion system secretin component, BpfG protease, BpfD putative c-di-GMP effector. **h** Current density at different stages. Stage I: inoculation of the strain SDV3 cells poised at 0.24 V (*vs*. the standard hydrogen electrode) until the current was stable. Stage II: the strain SDV3 cells were reset into a fresh medium in the absence of the inducer IPTG, thus PCA biosynthesis ceased and the PCA-mediated EET pathway was thus disrupted. Results in (**a**, **d**, and **f**) from three independent experiments ($n = 3$) were expressed as means and standard errors, and data in (**a**, **d**, and **f**) are shown as the mean ± SD. The results in (**b**, **c**, **e**, and **h**) have been checked for consistency with 3 individual experiments. Source data are provided as a Source Data file.

biosynthesis ceased, which led to the disruption of PCA-mediated EET. Then, the oxidation current dramatically dropped to 129.10 μA cm^{-2} (stage II, Fig. 5h). It was thus indicated PCA acting as the electron shuttle was the dominant mechanism underlying PCA-boosted EET in *S. oneidensis*.

Discussion

In this study, we found that exogenous addition of phenazine-1-carboxylic acid (PCA) at ~80 μM resulted in the highest power generation in *S. oneidensis* MR-1 than other shuttles (flavins and quinones) (Fig. 1a), which inspired us to program a PCA-mediated EET pathway in

S. oneidensis MR-1 via constructing PCA de novo biosynthesis pathway, facilitating PCA transport, and dynamically decoupling PCA biosynthesis and transport. These efforts achieved a substantial increase in EET in the engineered strain SDV3. Furthermore, we conducted comprehensive analyses of cellular electrophysiology, metabolism, and behavior to elucidate the mechanisms underlying the PCA-boosted EET.

To establish the PCA biosynthesis pathway and maintain the PCA level at ~80 μM in *S. oneidensis* MR-1, 11 native PCA biosynthesis operons were individually cloned into *S. oneidensis* MR-1. Among them, strain SC7 (P_{lacUV5}-*phzABCDEFG*) bearing the *phzABCDEFG* (originating from *P. aeruginosa* PAO1) produced the highest PCA level of 8.72 ± 0.76 μM and exhibited the highest EET rate with the maximum power density of 1185.93 ± 63.46 mW m^{-2}, 14.07-fold higher than that of the WT strain (84.30 ± 2.53 mW m^{-2}) (Fig. 1c and d). To further improve the PCA synthesis level, three promoters, including P_{ae}, P_{xyl}, and P_{tac}, were then individually assembled into strain SC7 to replace the promoter P_{lacUV5}, resulting in three recombinant strains SO1-SO3. Notably, strain SO3 (P_{tac}-*phzABCDEFG*) produced PCA at a level of 72.74 ± 4.30 μM (Fig. 1e), which was close to the optimal PCA level (~80 μM) and generated a maximum power density of 1757.87 ± 28.91 mW m^{-2} (Fig. 1f). The PCA biosynthesis was implemented in other microorganisms (including *E. coli*[76,77], *P. putida*[78], and cyanobacterium[79]) to enhance EET, however, the precise regulation of PCA biosynthesis level and the dose-dependent manner of PCA in mediating EET had not been systematically investigated in previous studies, thereby restricting the previous studies from accomplishing the full potential of PCA in efficiently facilitating EET.

To facilitate intracellular PCA transport out of cell to enhance EET, the porin OprF was expressed in strain SO3 to increase its cell membrane permeability. The obtained strain SP1 (P_{tac}-*phzABCDEFG* and P_{lacUV5}-*oprF*) exhibited a maximum power density of 2262.45 ± 10.92 mW m^{-2}, 1.29-fold higher than that of the strain SO3 (Fig. 2b). The analyses of cellular electrophysiology revealed that the intracellularly biosynthesized PCA was transported out of cell with the assistance of OprF, subsequently undergoing reduction by the outer membrane *c*-Cyts (MtrC and OmcA) and shuttling electrons to electrode, thus accelerating EET. It was demonstrated in previous studies that the porin, such as OprF, could accelerate the transmembrane transfer of flavins (as electron shuttles), and OprF was employed for enhancing EET[80–82]. Nevertheless, the electrophysiological mechanism underlying the acceleration of EET facilitated by OprF in conjunction with electron shuttles and *c*-Cyts has not been systematically elucidated. Furthermore, our study found that strain SP1 exhibited a significant reduction in cell growth rate compared to its parental strain SO3, unveiling an additional engineering issue related to the OprF cytotoxicity.

To relieve the OprF cytotoxicity, a PCA biosensor-based dynamic regulatory strategy was developed to decouple PCA biosynthesis and transport (Fig. 3a). Initially, PCA was synthesized, while OprF was not expressed. Once PCA reached a threshold detected by the PCA biosensor, the expression of OprF was subsequently initiated to facilitate the transport of PCA out of the cells. To this end, we developed a PCA biosensor P_{soxR}-*soxR*-P_{soxS} to construct the strain SD1 (P_{tac}-*phzABCDEFG* and P_{soxR}-*soxR*-P_{soxS}-*oprF*). However, due to the tardiness and weakness of the OprF expression regulated by the PCA biosensor P_{soxR}-*soxR*-P_{soxS}, the EET rate of strain SD1 was inhibited, the power density of which (1797.64 ± 53.40 mW m^{-2}) was lower than its parental strain SP1 (2262.45 ± 10.92 mW m^{-2}) (Fig. 3b). To address this issue, we further adopted a site-specific mutagenesis approach to optimize the PCA biosensor to achieve appropriate response strength and sensitivity, resulting in 9 PCA biosensor variants P_{soxR}-*soxR*-P_{soxS} V1-V9. These PCA biosensors were used to construct nine recombinant strains SDV1-9, in which the strain SDV3 (P_{tac}-*phzABCDEFG* and P_{soxR}-*soxR*-P_{soxS} V3-*oprF*) exhibited the highest EET rate with the maximum power density of 2845.26 ± 100.19 mW m^{-2}, 1.26- and 33.75-fold greater than that of the strain SP1 (2262.45 ± 10.92 mW m^{-2}) and WT (84.30 ± 2.53 mW m^{-2}), respectively (Fig. 3b). To the best of our knowledge, this is one of the highest recorded output power densities achieved by recombinant exoelectrogens[3,9,53,54].

Finally, the molecular mechanisms underlying PCA-boosted EET were elucidated. We found PCA could enhance lactate metabolism, *c*-Cyts biosynthesis, and biofilm formation via up-regulating the cAMP level (Fig. 5g), which partially contributed to the PCA-boosted EET in *S. oneidensis*. Furthermore, we identified that PCA as the electron mediator to shuttle electrons from OM *c*-Cyts to electrode was the dominant mechanism underlying the PCA-boosted EET. Intracellular electrons were transferred to extracellular PCA molecules through the OM *c*-Cyts MtrC and OmcA in a PCA dose-dependent manner. At low concentrations, PCA acted as a cofactor that bound to MtrC and OmcA to facilitate EET. With the increase in the PCA concentration, the PCA binding sites within MtrC and OmcA became saturated, and excess PCA conducted EET via diffusion in a free state. Overall, this study demonstrated that dynamic synthesis and transport of PCA was an efficient strategy to promote EET of *S. oneidensis*.

Methods

Bacterial culture

All of strains used in this work were cultured in Luria-Bertani (LB) medium with agitation. The temperature used was 37 °C for *E. coli* and 30 °C for *S. oneidensis*. When needed, related antibiotics, including 50 μg mL^{-1} kanamycin for pYYD, 50 μg mL^{-1} chloramphenicol for pHG13, and 15 μg mL^{-1} gentamicin for pHG1.0, were added for plasmid maintenance. Especially, *E. coli* WM3064 growth necessitated 2,6-diaminopimelic acid at the concentration of 100 μg mL^{-1}.

Gene synthesis and plasmid construction

The genes for PCA biosynthesis, transport, and PCA sensing were screened and excavated from NCBI database. After gene sequence codon optimization with an online tool (http://www.jcat.de/), the designed open reading frame with promoter and RBS was synthesized in vitro (GENEWIZ, China) and assembled into plasmid pYYD, pHG13 or pHG1.0 (Supplementary Fig. 25), respectively. All plasmid constructions were performed in *E. coli* DH5α. The *E. coli* WM3064 was employed to transfer plasmids into *S. oneidensis* strain through conjugation.

PCA measurement

The PCA concentration was measured using the high-performance liquid chromatography (HPLC) (Waters, E2695, USA). Supernatants and cells of bacterial culture were collected respectively. Cells were disrupted by sonication to release the intracellular PCA, which was subsequently mixed with supernatants. The PCA in this mixture was extracted with ethyl acetate. After separation, the ethyl acetate phase was evaporated at room temperature. The dried PCA was resuspended with methanol and then analyzed with HPLC. In HPLC analysis, the mixed mobile phase consisting of 5 mM ammonium acetate (40 %) and methanol (60 %) flowed through a C18 analytical column (100 mm, 2.1 mm, 2.6 mm, Thermo Scientific) at 0.7 mL min^{-1}. PCA was detected using a UV detector at 254 nm.

Confocal Raman measurements of *c*-Cyts

The anodic biofilms and purified *c*-Cyts (MtrC and OmcA) were placed onto slides. The LabRam HR Evolution (Horiba, France) was used for confocal Raman measurements at room temperature. Raman spectra were obtained with an excitation wavelength of 532 nm.

Green fluorescent protein (GFP) assay

A total of 200 μL of the sample was diluted with sterile saline (0.9% NaCl) to bring the fluorescence readings within the linear detection range. Fluorescence intensity was measured using an excitation wavelength of 485 nm and an emission wavelength of 520 nm, alongside cell density measurements (OD_{600}). These measurements were carried out in 96-well black polystyrene plates with clear bottoms using a SpectraMax M2 Microplate Reader (Molecular Devices, China). The relative fluorescence intensity was normalized using OD_{600}. Experiments were performed in three biological replicates.

The measurement of cell growth profile

During the incubation, a sample was taken and diluted into the linear range of the detector using sterile saline (0.9% NaCl). The optical density (OD) at 600 nm (OD_{600}) was measured for the estimation of cell density using a UV-Vis spectrophotometer (TU-1810).

The assessment of cell viability

Bacterial cells were collected by centrifugation (3024 × g, Avanti J-26S XP, Beckman Coulter, 4 °C, 10 min) and resuspended in sterile saline (0.9% NaCl). Subsequently, their optical density at 600 nm (OD_{600}) was standardized to 1. Following 10^4-fold dilution, the viable cell count was determined using the plate count method.

Transcriptomic analysis

Cells were harvested from the anode via centrifugation (4 °C, 7741 × g, Avanti J26S XP, Beckman Coulter, 30 min), which were immediately frozen in liquid nitrogen. The RNAprep pure Cell/Bacteria Kit (TIANGEN) was used to extract the total RNA. To prevent RNA degradation, lysozyme treatment was conducted and the isolated RNA was monitored on 1% agarose gels. The Qubit® RNA Assay Kit in Qubit® 2.0 Fluorometer (Life Technologies, CA, USA) and the 2100 Bioanalyzer (Agilent Technologies, CA, USA) were used to assess the RNA concentration and integrity, respectively. After removing rRNA using Ribo-zero kit, the residual mRNA acted as an input in a total of 3 μg per sample. The NEBNext®Ultra™ RNA Library Prep Kit for Illumina® (NEB, USA) was used to construct the sequencing libraries, in which each sample was modified with the index codes. The index-coded samples were clustered using the TruSeq PE Cluster Kit v3-cBot-HS (Illumina) on a cBot Cluster Generation System. The paired-end reads were generated with the sequencing of the library preparations on an Illumina HiSeq 4000 platform. Data analysis was performed by Beijing Novogene Bioinformatics Technology Co., Ltd (China).

RT-qPCR analysis

The mRNA extraction was conducted as the procedures in the "Transcriptomic analysis" section, and it was subsequently transformed into cDNA. The cDNA was synthesized through the GoScript Reverse Transcription System (Promega, USA). Target gene expression was quantified through the Sso Advanced SYBR Green Supermix (Bio-Rad, USA). The *gyrB* acts as the reference gene, of which the expression level was used to normalize the expression levels of the target genes. Primers used for the amplification of target gene are displayed in Supplementary Table 3. The $2^{-\Delta\Delta Ct}$ method[83] was used for data analysis.

Construction of mutant strains

Gene deletion mutants were made by using a suicide vector[84]. In brief, the right and left homology arms containing *attB* of the gene of interest were amplified from the genome, respectively, and were then fused by overlap PCR. The fused fragment was cloned into suicide plasmid pHG1.0 using Gateway BP Clonase enzyme (Invitrogen, USA) and the resulting vectors were transferred into *S. oneidensis* MR-1 via conjugation. Mutants with the first cross-over were selected with gentamicin (15 μg mL^{-1}) and verified by colony PCR. Verified transconjugants were grown on the LB agar plates with 10% sucrose. The sucrose-resistant colonies were analyzed by PCR and sequenced to verify removal of target genes.

Purification of *c*-Cyts OmcA and MtrC

The purification of *c*-Cyts OmcA and MtrC was performed according to the previous work[85]. Briefly, the recombinant *S. oneidensis* MR-1 strains for MtrC and OmcA production (obtained from Shi Lab) were inoculated into terrific broth until the OD_{600} of the culture reached 0.6, and then L-arabinose was added with the final concentration of 1 mM to induce *c*-Cyts synthesis over the following 17 h. The proteins were then transferred from culture supernatant into ice-cold Buffer A (20 mM HEPES, pH 7.8, 150 mM NaCl). The buffer A containing *c*-Cyts was loaded onto a Ni-Sepharose column (Ni Sepharose™ High Performance, Sigma). Subsequently, the *c*-Cyts was gradient-eluted from Ni-Sepharose column using Buffer B (buffer A + 10% glycerol + 10 mM imidazole), Buffer C (buffer A + 40 mM imidazole), and Buffer D (buffer A + 250 mM imidazole), respectively.

Quantitative and qualitative analyses of biofilm

The LIVE/DEAD Baclight bacterial viability kit (Invitrogen) was used to stain the biofilm. After incubation for 20 min with protection from light, the CLSM (Carl Zeiss Confocal Laser Scanning Microscopy LSM 780) was used to observe the biofilm confocal images. The biofilm on carbon cloth anode was first pretreated by fixing (2.5 % glutaraldehyde), dehydrating (25 %, 50 %, 75 %, 95 %, and 100 % ethanol solutions) and vacuum drying. After coating with Au, samples were subjected to the SEM imaging (APREO, FEI). The anode with biofilm was placed into sterile saline (0.9% NaCl), which was vortexed for cell isolation. The solutions containing cells were subjected to gradient dilution, which were then spread onto LB agar plates for CFU counting. The anode with biofilm was placed into a NaOH solution (0.2 M) and vortexed, which was then heated to lyse cells. After it had cooled to room temperature, the collected biomass was measured using the BCA Protein Assay Kit (Invitrogen, USA).

Measurement of the electron transfer kinetics between *c*-Cyts and PCA

The *c*-Cyts proteins and solutions of the PCA (80 μM) were diluted using 20 mM potassium phosphate buffer (pH 7.2) with 100 mM KCl. The MtrC and OmcA concentrations were adjusted to 1 μM based on their extinction coefficients (ε_{409nm} of 1670000 mol^{-1} L^{-1} cm^{-1} for OmcA and ε_{409nm} of 1440000 mol^{-1} L^{-1} cm^{-1} for MtrC)[86]. All reaction solutions were degassed with N_2 gas. MtrC and OmcA were gradually reduced with the concentrated sodium dithionite. The reductions were monitored with a UV-Vis spectrometer to avoid over-reduction. A stopped-flow spectrometer (SX20, Applied Photophysics Ltd, UK) was used for kinetic experiments, in which the 20 mM potassium phosphate buffer (pH 7.2) with 100 mM KCl was set as the buffer control. The temperature was kept at 30 °C and data were collected by measuring the light absorption changes at 552 nm.

UV-vis spectrophotometer measurement of *c*-Cyts

The cell cultures were collected and their OD_{600} was adjusted to 3.0. Through centrifugation (17,418 × g, Avanti J26S XP, Beckman Coulter, 5 min), the supernatant was removed and the cell pellets were resuspended in PBS (10 mM). The resuspended cells were lysed by ultrasonication in an ice bath (200 W, ultrasonication−2 s - waiting- 1 s cycle for 30 min) with an Ultrasonic Homogenizer (Scientz, China). The *c*-Cyts in cell lysate were measured using a microplate reader (Scientz, China).

SDS-PAGE with heme staining of *c*-Cyts

The cell cultures were collected and their OD_{600} was adjusted to 10.0. Through centrifugation (17,418 × g, Avanti J26S XP, Beckman Coulter, 5 min), the supernatant was removed. And the collected cell pellets were washed with sterilized 10 mM PBS buffer (pH 7.2) for three times. The cells were resuspended in 160 μL distilled water with 40 μL of 5 × loading dye. The loading dye consists of 0.25 M Tris-HCl, pH 6.8, 50% (v/v) glycerol, 10% (w/v) SDS, and 0.5% (w/v) bromophenol blue. The resuspension was treated at 96 °C in a hot water bath for 10 min. After cooling to room temperature, 20 µL of the suspended cells were loaded on 12% (w/v) polyacrylamide gels for electrophoresis, and then run at 150 V for ~1 h on a Bio-Rad Mini-PROTEAN Tetra Cell System. The electrophoresis running buffer contains 3.03 g L^{-1} Tris, 18.8 g L^{-1} glycine, and 1 g L^{-1} SDS. After electrophoresis, the gels were immersed in a solution that contains 30 mL of 6.3 mM 3,3′,5,5′-tetramethylbenzidine (TMBZ) dissolved in methanol and 70 mL of 0.25 M sodium acetate (pH 5.0). After incubating overnight in the dark at 4 °C, 3 mL of 30% hydrogen peroxide was added and staining became visible within 30 min[87]. The stained gels were imaged using Imagelab (Bio-Rad) software.

Lactate measurement

Biosensor Analyzer (SBA-40E) was used to measure the lactate concentration with 50 mg mL^{-1} lactate as standard.

Intracellular cAMP concentration measurement

The cell pellets were collected via centrifugation (17,418 × g, Avanti J26S XP, Beckman Coulter, 10 min, 4 °C) and resuspended into pre-cooling buffer comprising of methanol, acetonitrile and ddH_2O (2:2:1, v/v/v). The cells were lysed by ultrasonication in an ice bath (200 W, ultrasonicating-2 s-waiting-1 s cycle for 30 min) with an Ultrasonic Homogenizer (Scientz, China), and the intracellular cAMP was released into the supernatant for collection. Meanwhile, the biomass of lysed cells was measured using the BCA protein assay kit (Invitrogen, USA). Subsequently, the cAMP was concentrated via freeze drying and devoted into concentration measurement using liquid chromatography-mass spectrometry (LC-MS)[88]. In these processes, the 2 ng mL^{-1} of 8-bromoadenosine (8-bromo-cAMP) was set as internal standard. The Ultra Performance Liquid Chromatography-triple quadrupole tandem mass spectrometry (Waters, XEVO-TQ-XS) was used to detect cAMP. The chromatographic separation was performed at 25 °C using a C18 analytical column (100 mm, 2.1 mm, 2.6 mm, Thermo Scientific) and a flow rate of 0.4 mL min^{-1}. The mobile phase was 75% A (water containing 0.1% acetic acid) and 25% B (acetonitrile 90% with 0.1% acetic acid). The injection volume was 10 µL of each sample. The mass spectrometer, equipped with an electrospray (ESI) source in the negative polarity mode (ESI^-), was configured for multiple reaction monitoring to monitor the transitions 328.10 > 134.30 *m/z* for cAMP and 407.90 > 214.15 *m/z* for 8-bromo-cAMP. Finally, the intracellular cAMP concentration was normalized to the protein biomass measured by BCA assay kit.

Simulation of interaction between MtrC or OmcA and PCA

A semi-flexible docking system was employed for docking simulations using Autodock Vina[89]. The protein crystallographic structures (4LMH for OmcA and 4LM8 for MtrC) were obtained from Protein Data Bank, PDB and the electron shuttle's molecular structure (2538-68-3 for PCA) was downloaded from Pub-Chem molecular database (http://pubchem.ncbi.nlm.nih.gov/). During simulations, the searching spaces of MtrC and OmcA were both limited to a grid box within 30 × 30 × 30 Å, centering at the hemes 2, 7, and 10 of MtrC, and hemes 5, and 10 of OmcA, respectively. Ten possible docking models were recorded from each simulation and the same interaction was simulated three times.

Construction of PCA sensor with point mutation

The SnaB I and Xcm I restriction sites were added into the target region in the plasmid by reverse PCR. The target region was then removed by treatment with SnaB I and Xcm I restriction enzymes. The in vitro manufactured DNA fragment with the mutation and SnaB I and Xcm I sites was ligated to the plasmid whose target region was removed with SnaB I and Xcm I restriction enzymes.

The assessment of cell membrane permeability

The bacterial cells were added into PBS buffer at a final OD_{600} of 0.5. The N-phenyl-1-naphthylamine was then added into the cell suspension at final concentration of 6 µM. After incubation for 10 min at 30 °C, the microplate reader was used to record the fluorescence emission (scanning from 400 to 500 nm) with excitation at 355 nm.

The calculation of dissociation constant (K_d) in the interactions between PCA and *c*-Cyts

The K_d was calculated according to the protein-ligand binding model (as shown in Eqs. (1–4)) developed by Okamoto et al.[64].

$$\mathrm{PCA}-c-\mathrm{Cyts(PL)} \rightleftharpoons \mathrm{PCA(L)}+c-\mathrm{Cyts(P)} \tag{1}$$

$$\mathrm{K_d}=\frac{[P][L]}{[PL]} \tag{2}$$

$[P]$, $[L]$, and $[PL]$ are the concentration of *c*-Cyts, soluble PCA, and the PCA−*c*-Cyts complex, respectively. Under different PCA concentrations of $[L]_1$ and $[L]_2$, the relationship of peak currents (I_{P1} and I_{P2}) of the bound PCA in DPV measurements between the concentration of PCA−*c*-Cyts complex ($[PL]_1$ and $[PL]_2$) was shown as the Eq. 3.

$$\frac{I_{P2}}{I_{P1}}=\frac{[PL]_2}{[PL]_1}=\alpha \tag{3}$$

By using these equations, K_d could be described as Eq. 4.

$$\mathrm{K_d}=\frac{(\alpha-1)[L]_1}{1-\alpha\frac{[L]_1}{[L]_2}} \tag{4}$$

Briefly, PCA with the final concentration of 2 µM ($[L]_1$) was firstly added into the three-electrode test reactor for electrochemical cultivation of the strains (wild-type *S. oneidensis* MR-1 and the *c*-Cyts Ala mutants). After achieving a stabilized output current, the DPV measurements (-0.395 V to -0.1 V (*vs.* Ag/AgCl), scan rate of 1 mV/s, and a step size of 5 mV) were conducted for obtaining the peak current I_{p1} of the bound PCA. Subsequently, the PCA concentration was further up-regulated to 4 µM ($[L]_2$) with subsequent electrochemical cultivation in the three-electrode test reactor. Upon the occurrence of the stabilized output current, once again, the DPV measurement was conducted for obtaining the I_{p2}.

Microbial fuel cell setup

An H-type two-chamber cell (140 mL working volume) was used to set up the microbial fuel cell, in which Nafion 117 membrane, acting as proton exchange membrane, separated anode and cathode. In the anodic chamber, a 1 cm × 1 cm carbon cloth was made the anodic electrode. In the cathodic chamber, a 2.5 cm × 3 cm carbon cloth was made the cathodic electrode and 50 mM potassium ferrocyanide dissolving in 50 mM phosphate buffer (50 mM K_2HPO_4 and 50 mM KH_2PO_4) was used as cathodic electron donor. The overnight-cultured bacterial cells were inoculated into the anode compartment, which were fed with anodic medium (M9 buffer, 5% LB broth, 20 mM lactate, pH 7.2) and induced by isopropyl-β-D-thiogalactoside (IPTG, 0.5 mM). To expedite the preparation of bacterial cells for testing, cell growth was enhanced through magnetic stirring over a period of 10 h. Following this, normalization was performed for anodic biomass (OD_{600} of 0.7), the anodic electron donor (lactate at a concentration of 20 mM), and the cathodic electron acceptor (potassium ferrocyanide at a concentration of 5 mM). These strains were finally subjected to bioelectrochemical measurements at 30 °C.

Electrochemical analyses

Using a CHI 1000 C multichannel electrochemical workstation (CH Instruments, Shanghai, China), the linear sweep voltammetry (LSV) analysis was employed to obtain the polarization curves for maximum power density calculation. In LSV, the scan rate was set to 0.1 mV s^{-1}. The power density (P) was calculated using Eq. 5.

$$P = \frac{V \times I}{S} \tag{5}$$

where V is the voltage; I is the current, and S is the projected area of the anode.

The MFC internal resistance analysis was conducted through the electrochemical impedance spectroscopy (EIS) on PGSTAT 302 N electrochemical workstation (Metrohm Autolab, Switzerland). In EIS testing, the carbon cloth anode was set as the working electrode. The Pt wire and Ag/AgCl were set as the counter electrode and the reference electrode, respectively. The EIS was measured within the frequency range of 0.01 kHz – 100 kHz at an potential (vs. Ag/AgCl).

In differential pulse voltammetry (DPV) measurements, the strains, including wild-type *S. oneidensis* MR-1 (WT) and mutants WTΔ*mtrC*, WTΔ*omcA*, and WTΔ*mtrC*Δ*omcA*, were first conducted electrochemical cultivation in three-electrode system with the addition of PCA in various concentration, in which the Ag/AgCl was set as the reference electrode, the carbon cloth (1 cm × 1 cm) was as set as the working electrode and Pt wire was set as the counter electrode. During anaerobic operation, the overnight cultured bacterial cells were added to the anodic medium at a final OD_{600} of 0.7, and the working electrode was poised at 0 V (*vs.* Ag/AgCl) using the potentiostat (CHI1000C, CH Instruments, Shanghai, China). The DPV was carried out using CHI 660E electrochemical workstation (CH Instruments, Shanghai, China) after achieving a stabilized output current, which was conducted within a scanning window ranging from -0.5 to -0.1 V (*vs.* Ag/AgCl), employing a scan rate of 1 mV/s, a period of 1 s, a pulse time of 0.5 s, a pulse width of 50 mV, and a step size of 1 mV. The DPV measurements were also performed on the abiotic PCA-containing medium sample using the same parameters.

Reporting summary

Further information on research design is available in the Nature Portfolio Reporting Summary linked to this article.

Data availability

The data supporting the findings of this study are available within the paper and its Supplementary Information files. A reporting summary for this article can also be found as a Supplementary Information file. The transcriptome data generated in this study have been deposited in Gene Expression Omnibus under accession GSE289377. Source data are provided with this paper.

References

1. Chen, H. et al. Fundamentals, applications, and future directions of bioelectrocatalysis. *Chem. Rev.* **120**, 12903–12993 (2020).
2. Kumar, A. et al. The ins and outs of microorganism-electrode electron transfer reactions. *Nat. Rev. Chem.* **1**, 0024 (2017).
3. Logan, B. E., Rossi, R., Ragab, A. & Saikaly, P. E. Electroactive microorganisms in bioelectrochemical systems. *Nat. Rev. Microbiol.* **17**, 307–319 (2019).
4. Lu, L. et al. Wastewater treatment for carbon capture and utilization. *Nat. Sustain.* **1**, 750–758 (2018).
5. Logan, B. E. & Rabaey, K. Conversion of wastes into bioelectricity and chemicals by using microbial electrochemical technologies. *Science* **337**, 686–690 (2012).
6. Williams, K. H., Bargar, J. R., Lloyd, J. R. & Lovley, D. R. Bioremediation of uranium-contaminated groundwater: a systems approach to subsurface biogeochemistry. *Curr. Opin. Biotechnol.* **24**, 489–497 (2013).
7. Lovley, D. R., Phillips, E. J. P., Gorby, Y. A. & Landa, E. R. Microbial reduction of uranium. *Nature* **350**, 413–416 (1991).
8. Liu, X. et al. Power generation from ambient humidity using protein nanowires. *Nature* **578**, 550–554 (2020).
9. Cao, B. et al. Silver nanoparticles boost charge-extraction efficiency in *Shewanella* microbial fuel cells. *Science* **373**, 1336–1340 (2021).
10. Chen, X. et al. Electrical decoupling of microbial electrochemical reactions enables spontaneous H_2 evolution. *Energy Environ. Sci.* **13**, 495–502 (2020).
11. Logan, B. E., Shi, L. & Rossi, R. Enabling the use of seawater for hydrogen gas production in water electrolyzers. *Joule* **5**, 760–762 (2021).
12. Guo, J. et al. Light-driven fine chemical production in yeast biohybrids. *Science* **362**, 813–816 (2018).
13. Sakimoto, K. K., Wong, A. B. & Yang, P. Self-photosensitization of nonphotosynthetic bacteria for solar-to-chemical production. *Science* **351**, 74–77 (2016).
14. Liu, X. & Yu, X. Enhancement of butanol production: from biocatalysis to bioelectrocatalysis. *ACS Energy Lett.* **5**, 867–878 (2020).
15. Li, H. et al. Integrated electromicrobial conversion of CO_2 to higher alcohols. *Science* **335**, 1596 (2012).
16. Tian, L. J. et al. Directed biofabrication of nanoparticles through regulating extracellular electron transfer. *J. Am. Chem. Soc.* **139**, 12149–12152 (2017).
17. Choi, Y. & Lee, S. Y. Biosynthesis of inorganic nanomaterials using microbial cells and bacteriophages. *Nat. Rev. Chem.* **4**, 638–656 (2020).
18. Fan, G., Graham, A. J., Kolli, J., Lynd, N. A. & Keitz, B. K. Aerobic radical polymerization mediated by microbial metabolism. *Nat. Chem.* **12**, 638–646 (2020).
19. Fan, G., Dundas, C. M., Graham, A. J., Lynd, N. A. & Keitz, B. K. *Shewanella oneidensis* as a living electrode for controlled radical polymerization. *Proc. Natl. Acad. Sci. USA.* **115**, 4559–4564 (2018).
20. Chen, X., Cao, Y., Li, F., Tian, Y. & Song, H. Enzyme-assisted microbial electrosynthesis of poly(3-hydroxybutyrate) via CO_2 bioreduction by engineered *Ralstonia eutropha*. *ACS Catal.* **8**, 4429–4437 (2018).
21. Atkinson, J. T. et al. Real-time bioelectronic sensing of environmental contaminants. *Nature* **611**, 548–553 (2022).
22. Choi, S. Electrogenic bacteria promise new opportunities for powering, sensing, and synthesizing. *Small* **18**, e2107902 (2022).
23. Rezaie, M., Rafiee, Z. & Choi, S. A biobattery capsule for ingestible electronics in the small intestine: biopower production from intestinal fluids activated germination of exoelectrogenic bacterial endospores. *Adv. Energy Mater.* **13**, 2202581 (2022).
24. Shi, L. et al. Extracellular electron transfer mechanisms between microorganisms and minerals. *Nat. Rev. Microbiol.* **14**, 651–662 (2016).
25. Reguera, G. et al. Extracellular electron transfer via microbial nanowires. *Nature* **435**, 1098–1101 (2005).
26. Lovley, D. R. & Holmes, D. E. Electromicrobiology: the ecophysiology of phylogenetically diverse electroactive microorganisms. *Nat. Rev. Microbiol.* **20**, 5–19 (2022).
27. Saunders, S. H. et al. Extracellular DNA promotes efficient extracellular electron transfer by pyocyanin in *Pseudomonas aeruginosa* Biofilms. *Cell* **182**, 919–932 e919 (2020).
28. Newman, D. K. & Kolter, R. A role for excreted quinones in extracellular electron transfer. *Nature* **405**, 94–97 (2000).
29. Marsili, E. et al. *Shewanella* secretes flavins that mediate extracellular electron transfer. *Proc. Natl. Acad. Sci. USA.* **105**, 3968–3973 (2008).

30. Glasser, N. R., Saunders, S. H. & Newman, D. K. The colorful world of extracellular electron shuttles. *Annu. Rev. Microbiol.* **71**, 731–751 (2017).
31. Zhao, J. et al. Microbial extracellular electron transfer and strategies for engineering electroactive microorganisms. *Biotechnol. Adv.* **53**, 107682 (2021).
32. Chukwubuikem, A., Berger, C., Mady, A. & Rosenbaum, M. A. Role of phenazine-enzyme physiology for current generation in a bioelectrochemical system. *Microb. Biotechnol.* **14**, 1613–1626 (2021).
33. Glasser, N. R., Wang, B. X., Hoy, J. A. & Newman, D. K. The pyruvate and alpha-ketoglutarate dehydrogenase complexes of *Pseudomonas aeruginosa* catalyze pyocyanin and phenazine-1-carboxylic acid reduction via the subunit dihydrolipoamide dehydrogenase. *J. Biol. Chem.* **292**, 5593–5607 (2017).
34. Coursolle, D., Baron, D. B., Bond, D. R. & Gralnick, J. A. The Mtr respiratory pathway is essential for reducing flavins and electrodes in *Shewanella oneidensis*. *J. Bacteriol.* **192**, 467–474 (2010).
35. Wu, Y. et al. Enhanced current production by exogenous electron mediators via synergy of promoting biofilm formation and the electron shuttling process. *Environ. Sci. Technol.* **54**, 7217–7225 (2020).
36. Rabaey, K., Boon, N., Hofte, M. & Verstraete, W. Microbial phenazine production enhances electron transfer in biofuel cells. *Environ. Sci. Technol.* **39**, 3401–3408 (2005).
37. von Canstein, H., Ogawa, J., Shimizu, S. & Lloyd, J. R. Secretion of flavins by *Shewanella* species and their role in extracellular electron transfer. *Appl. Environ. Microbiol.* **74**, 615–623 (2008).
38. Okamoto, A., Hashimoto, K. & Nealson, K. H. Flavin redox bifurcation as a mechanism for controlling the direction of electron flow during extracellular electron transfer. *Angew. Chem. Int. Ed. Engl* **53**, 10988–10991 (2014).
39. Light, S. H. et al. A flavin-based extracellular electron transfer mechanism in diverse gram-positive bacteria. *Nature* **562**, 140–144 (2018).
40. Wang, Y., Kern, S. E. & Newman, D. K. Endogenous phenazine antibiotics promote anaerobic survival of *Pseudomonas aeruginosa* via extracellular electron transfer. *J. Bacteriol.* **192**, 365–369 (2010).
41. Glasser, N. R., Kern, S. E. & Newman, D. K. Phenazine redox cycling enhances anaerobic survival in *Pseudomonas aeruginosa* by facilitating generation of ATP and a proton-motive force. *Mol. Microbiol.* **92**, 399–412 (2014).
42. Min, D. et al. Extracellular electron transfer via multiple electron shuttles in waterborne Aeromonas hydrophila for bioreduction of pollutants. *Biotechnol. Bioeng.* **118**, 4670–4770 (2021).
43. Mevers, E. et al. An elusive electron shuttle from a facultative anaerobe. *eLife* **8**, e48054 (2019).
44. Rhodes, Z., Simoska, O., Dantanarayana, A., Stevenson, K. J. & Minteer, S. D. Using structure-function relationships to understand the mechanism of phenazine-mediated extracellular electron transfer in *Escherichia coli*. *iScience* **24**, 103033 (2021).
45. Mavrodi, D. V., Blankenfeldt, W. & Thomashow, L. S. Phenazine compounds in fluorescent *Pseudomonas spp*. biosynthesis and regulation. *Annu. Rev. Phytopathol.* **44**, 417–445 (2006).
46. Liu, J., Qiao, Y., Lu, Z. S., Song, H. & Li, C. M. Enhance electron transfer and performance of microbial fuel cells by perforating the cell membrane. *Electrochem. Commun.* **15**, 50–53 (2012).
47. Dietrich, L. E., Teal, T. K., Price-Whelan, A. & Newman, D. K. Redox-active antibiotics control gene expression and community behavior in divergent bacteria. *Science* **321**, 1203–1206 (2008).
48. Watanabe, S., Kita, A., Kobayashi, K. & Miki, K. Crystal structure of the [2Fe-2S] oxidative-stress sensor SoxR bound to DNA. *Proc. Natl. Acad. Sci. USA* **105**, 4121–4126 (2008).
49. Luirink, J. & Sinning, I. SRP-mediated protein targeting: structure and function revisited. *Biochim. Biophys. Acta* **1694**, 17–35 (2004).
50. Osborne, A. R., Rapoport, T. A. & van den Berg, B. Protein translocation by the Sec61/SecY channel. *Annu. Rev. Cell. Dev. Biol.* **21**, 529–550 (2005).
51. Andersson, H. & von Heijne, G. Sec dependent and sec independent assembly of *E. coli* inner membrane proteins: the topological rules depend on chain length. *EMBO J.* **12**, 683–691 (1993).
52. Wagner, S. et al. Consequences of membrane protein overexpression in *Escherichia coli*. *Mol. Cell. Proteomics* **6**, 1527–1550 (2007).
53. Yang, C. H. et al. Carbon dots-fed *Shewanella oneidensis* MR-1 for bioelectricity enhancement. *Nat. Commun.* **11**, 1379 (2020).
54. Liu, X. et al. Microbial biofilms for electricity generation from water evaporation and power to wearables. *Nat. Commun.* **13**, 4369 (2022).
55. Paquete, C. M. et al. Exploring the molecular mechanisms of electron shuttling across the microbe/metal space. *Front. Microbiol.* **5**, 318 (2014).
56. Neto, S. E., de Melo-Diogo, D., Correia, I. J., Paquete, C. M. & Louro, R. O. Characterization of OmcA mutants from *Shewanella oneidensis* MR-1 to investigate the molecular mechanisms underpinning electron transfer across the microbe-electrode interface. *Fuel Cells* **17**, 601–611 (2017).
57. Okamoto, A., Hashimoto, K., Nealson, K. H. & Nakamura, R. Rate enhancement of bacterial extracellular electron transport involves bound flavin semiquinones. *Proc. Natl. Acad. Sci. USA* **110**, 7856–7861 (2013).
58. Okamoto, A. et al. Cell-secreted flavins bound to membrane cytochromes dictate electron transfer reactions to surfaces with diverse charge and pH. *Sci. Rep.* **4**, 5628 (2014).
59. Okamoto, A. et al. Uptake of self-secreted flavins as bound cofactors for extracellular electron transfer in *Geobacter* species. *Energy Environ. Sci.* **7**, 1357–1361 (2014).
60. Xu, S., Jangir, Y. & El-Naggar, M. Y. Disentangling the roles of free and cytochrome-bound flavins in extracellular electron transport from *Shewanella oneidensis* MR-1. *Electrochim. Acta* **198**, 49–55 (2016).
61. Edwards, M. J., White, G. F., Butt, J. N., Richardson, D. J. & Clarke, T. A. The crystal structure of a biological insulated transmembrane molecular wire. *Cell* **181**, 1–9 (2020).
62. Jiang, X. et al. Kinetics of trifurcated electron flow in the decaheme bacterial proteins MtrC and MtrF. *Proc. Natl. Acad. Sci. USA* **116**, 3425–3430 (2019).
63. Edwards, M. J. et al. The X-ray crystal structure of *Shewanella oneidensis* OmcA reveals new insight at the microbe-mineral interface. *FEBS Lett.* **588**, 1886–1890 (2014).
64. Okamoto, A., Nakamura, R., Nealson, K. H. & Hashimoto, K. Bound flavin model suggests similar electron-transfer mechanisms in *Shewanella* and *Geobacter*. *ChemElectroChem* **1**, 1808–1812 (2014).
65. Gralnick, J. A., Vali, H., Lies, D. P. & Newman, D. K. Extracellular respiration of dimethyl sulfoxide by *Shewanella oneidensis* strain MR-1. *Proc. Natl. Acad. Sci. USA* **103**, 4669–4674 (2006).
66. Zhang, H., Han, K. & Hu, X. Enhanced bioreduction of 2,5-dichlorobenzene by an AHQ/RGO binary nanocomposite through a synergistic effect with outer membrane proteins of *Shewanella oneidensis* MR-1. *Chem. Eng. J.* **389**, 124464 (2020).
67. Liu, L., Wang, W., Wu, S. & Gao, H. Recent advances in the siderophore biology of *Shewanella*. *Front. Microbiol.* **13**, 823758 (2022).
68. Matsumoto, A., Koga, R., Kanaly, R. A., Kouzuma, A. & Watanabe, K. Identification of a diguanylate cyclase that facilitates biofilm formation on electrodes by *Shewanella oneidensis* MR-1. *Appl. Environ. Microbiol.* **87**, e00201–e00221 (2021).
69. Wu, L., Wang, J., Tang, P., Chen, H. & Gao, H. Genetic and molecular characterization of flagellar assembly in *Shewanella oneidensis*. *PLoS ONE* **6**, e21479 (2011).

70. McLean, J. S. et al. Oxygen-dependent autoaggregation in *Shewanella oneidensis* MR-1. *Environ. Microbiol.* **10**, 1861–1876 (2008).
71. Starwalt-Lee, R., El-Naggar, M. Y., Bond, D. R. & Gralnick, J. A. Electrolocation? The evidence for redox-mediated taxis in *Shewanella oneidensis*. *Mol. Microbiol.* **115**, 1069–1079 (2021).
72. Godeke, J., Paul, K., Lassak, J. & Thormann, K. M. Phage-induced lysis enhances biofilm formation in *Shewanella oneidensis* MR-1. *ISME J* **5**, 613–626 (2011).
73. Kasai, T., Kouzuma, A., Nojiri, H. & Watanabe, K. Transcriptional mechanisms for differential expression of outer membrane cytochrome genes *omcA* and *mtrC* in *Shewanella oneidensis* MR-1. *BMC Microbiol.* **15**, 68 (2015).
74. Wissig, J. et al. CyaC, a redox-regulated adenylate cyclase of *Sinorhizobium meliloti* with a quinone responsive diheme-B membrane anchor domain. *Mol. Microbiol.* **112**, 16–28 (2019).
75. Liu, C. et al. cAMP and c-di-GMP synergistically support biofilm maintenance through the direct interaction of their effectors. *Nat. Commun.* **13**, 1493 (2022).
76. Simoska, O. et al. Enhancing the performance of microbial fuel cells via metabolic engineering of *Escherichia coli* for phenazine production. *ACS Sustain. Chem. Eng.* **11**, 11855–11866 (2023).
77. Feng, J. et al. Direct electron uptake from a cathode using the inward Mtr pathway in *Escherichia coli*. *Bioelectrochemistry* **134**, 107498 (2020).
78. Askitosari, T. D., Boto, S. T., Blank, L. M. & Rosenbaum, M. A. Boosting heterologous phenazine production in *Pseudomonas putida* KT2440 through the exploration of the natural sequence space. *Front. Microbiol.* **10**, 1990 (2019).
79. Clifford, E. R. et al. Phenazines as model low-midpoint potential electron shuttles for photosynthetic bioelectrochemical systems. *Chem. Sci.* **12**, 3328–3338 (2021).
80. Yong, Y. C. et al. Enhancement of extracellular electron transfer and bioelectricity output by synthetic porin. *Biotechnol. Bioeng.* **110**, 408–416 (2013).
81. Lin, T. et al. Engineered *Shewanella oneidensis*-reduced graphene oxide biohybrid with enhanced biosynthesis and transport of flavins enabled a highest bioelectricity output in microbial fuel cells. *Nano Energy* **50**, 639–648 (2018).
82. Zhou, T. et al. A copper-specific microbial fuel cell biosensor based on riboflavin biosynthesis of engineered *Escherichia coli*. *Biotechnol. Bioeng.* **118**, 210–222 (2021).
83. Livak, K. J. & Schmittgen, T. D. Analysis of relative gene expression data using real-time quantitative PCR and the $2^{-\Delta\Delta C_T}$ method. *Methods* **25**, 402–408 (2001).
84. Jin, M. et al. Unique organizational and functional features of the cytochrome c maturation system in *Shewanella oneidensis*. *PLoS ONE* **8**, e75610 (2013).
85. Shi, L. et al. Isolation of a high-affinity functional protein complex between OmcA and MtrC: Two outer membrane decaheme *c*-type cytochromes of *Shewanella oneidensis* MR-1. *J. Bacteriol.* **188**, 4705–4714 (2006).
86. Ross, D. E., Brantley, S. L. & Tien, M. Kinetic characterization of OmcA and MtrC, terminal reductases involved in respiratory electron transfer for dissimilatory iron reduction in *Shewanella oneidensis* MR-1. *Appl. Environ. Microbiol.* **75**, 5218–5226 (2009).
87. Hartshorne, RobertS. et al. Characterization of an electron conduit between bacteria and the extracellular environment. *Proc. Natl. Acad. Sci. USA* **106**, 22169–22174 (2009).
88. Nash, C. E. S., Antunes, N. J., Coelho-Silva, W. C., Campos, R. & De Nucci, G. Quantification of cyclic AMP and cyclic GMP levels in Krebs-Henseleit solution by LC-MS/MS: application in washed platelet aggregation samples. *J. Chromatogr. B* **1211**, 123472 (2022).
89. Trott, O. & Olson, A. J. Software news and update AutoDock vina: improving the speed and accuracy of docking with a new scoring function, efficient optimization, and multithreading. *J. Comput. Chem.* **31**, 455–461 (2010).

Acknowledgements

This work was supported by the National Key Research and Development Program of China (2024YFC3407000 and 2018YFA0901300), the National Natural Science Foundation of China (NSFC 22378305, 32071411, 22478293, and 32001034), Tianjin Science and Technology Plan Project (24JCYBJC01120), and the Haihe Laboratory of Sustainable Chemical Transformations (24HHWCSS00004). We gratefully acknowledge the technical support from the Advanced Instrumental Analysis Center, School of Chemical Engineering and Technology, Tianjin University, for their provision of high-performance characterization services. Special thanks are extended to Shaolan Zou (Tianjin University) and Shengsong Yu (University of Science and Technology of China) for their expert assistance with measurements during this research.

Author contributions

F.L., and B.-C.Z. contributed equally to the work. F.L., and B.-C.Z. designed the project, analyzed data, and drafted the manuscript. B.-C.Z., X.-Z. L., H.Y., S.-C.S., Z.-X.Y., Q.-J.L., C.L., R.T., S.-B.W., X.-J.A., and Y.-X.L. performed experiments. L.S. and K.H.N. critically revised the manuscript. H.S. supervised the project, designed experiments, analyzed data, and critically revised the manuscript.

Competing interests

The authors declare no competing interests.

Additional information

Supplementary information The online version contains supplementary material available at https://doi.org/10.1038/s41467-025-57497-z.

Correspondence and requests for materials should be addressed to Hao Song.

Peer review information *Nature Communications* thanks Haichun Gao, Akihiro Okamoto and the other, anonymous, reviewer(s) for their contribution to the peer review of this work. A peer review file is available.

Reprints and permissions information is available at http://www.nature.com/reprints

Publisher's note Springer Nature remains neutral with regard to jurisdictional claims in published maps and institutional affiliations.